Composites Part B 260 (2023) 110735

Contents lists available at ScienceDirect

Composites Part B

journal homepage: www.elsevier.com/locate/compositesb

Non-linear analytical model for FRCM coupons in tension

Yu Yuan, Gabriele Milani *

Department of Architecture, Built Environment and Construction Engineering (ABC), Politecnico di Milano, Piazza Leonardo da Vinci 32, 20133, Milan, Italy

ARTICLE INFO

Handling Editor: Prof. Ole Thomsen

Keywords:
FRCM
Tensile test
Analytical solutions
Failure mechanism

ABSTRACT

Externally bonded FRCM (Fiber Reinforced Cementitious Matrix) materials are nowadays quite diffused to reinforce existing structures: taking as reference FRP (Fiber Reinforced Polymer), the replacement of an organic matrix with mortar is more compatible with masonry substrates, and the reversibility of the reinforcement is more appealing for the architectural heritage conservation. At the same time, due to the low strength of the mortar layers, complex failure mechanisms are observed for FRCMs, which still need comprehensive theoretical investigations. Indeed, not only the mortar-fiber interface may behave non-linearly, but also the mortar may crack and affect the overall behavior. The tensile test on coupons is commonly used as a direct approach to characterize the properties of the reinforcing package, and there is a wide consensus on approximating the global behavior with a trilinear law; however, the different test set-ups and the inhomogeneity of the material itself bring about large dispersion of the experimental results. This paper aims at proposing a simplified analytical model to consider the damage mechanisms in FRCM coupons in tension, including interface slippage, mortar cracking, and their simultaneous occurrence. The accuracy of the model is then verified by comparing the results with experimental data. The conditions under which such failure mechanisms occur and the effects of material properties are also investigated with a view to complement the understanding of experimental observations from a theoretical perspective.

1. Introduction

For many existing masonry buildings, which include also a great part of the architectural heritage, strengthening interventions are necessary to increase the structural safety. External bonding of composite materials to structural elements is a common and effective reinforcement strategy, considering the limited variation of weight and useable space, as well as the flexible and rapid application. In recent years, FRCM (Fiber Reinforced Cement Matrix), also known as TRM (Textile Reinforced Mortar) has attracted increasing attention, particularly for the reinforcement of masonry structures as an alternative to FRP (Fiber Reinforced Polymer). Instead of the organic matrix adopted in FRP strengthening, the inorganic matrix of FRCM ensures better compatibility with masonry materials, allows moisture evaporation, and performs better at high temperatures [1]. A further important advantage, especially for architectural heritage, is the reversibility.

As a critical aspect that has been emphasized in FRP-reinforced systems, the adhesion between the externally applied composite and the substrate is very important, since poor bonding will lead to premature failure of the reinforcing system without activating the full participation of the composite. Shear tests, which are commonly used to characterize bond behaviors, have also been conducted to investigate FRCM-reinforced samples [2,3]. However, unlike FRP materials (which typically exhibit higher strength), in addition to the detachment of the reinforcement from the substrate, failures inside the FRCM reinforcement can occur: the mortar may crack, the fiber textile may slide inside the mortar layers, and the fibers may be subjected to rupture. Therefore, the description of the failure mechanism developing inside an FRCM reinforcing package is an important open issue that deserves consideration. Tensile tests on coupons are widely used to characterize FRCM material properties; both Italian CNR-DT 215/2018 [4] and American ACI 549.6R-2020 [5] guidelines require testing standardized FRCM specimens in tension, for a preliminary evaluation of the system performance. On the other hand, many experimental campaigns have been carried out [3,6–16], including several Round Robin Tests containing both shear and tensile tests involving a variety of materials and experimental set-ups [17–20].

The results of tensile tests for FRCM often show a high degree of dispersion, which is due to many reasons, for instance, the irregularities of the specimens themselves, such as differences in casting dimensions,

* Corresponding author.
E-mail address: gabriele.milani@polimi.it (G. Milani).

https://doi.org/10.1016/j.compositesb.2023.110735
Received 26 January 2023; Received in revised form 3 April 2023; Accepted 12 April 2023
Available online 20 April 2023

misalignment of yarns, and the appearance of micro-cracks in the mortar. As a result of the specimens' inhomogeneities, the location where the first crack appears is also not fully predictable, resulting in inaccurate measurements when the range of displacement measuring devices (such as extensometers or LVDTs) is not sufficient to cover the crack development. In combination with conventional measuring devices, DIC [6,21,22] or buried sensors [9] have also been used to avoid this problem while obtaining more detailed information. On the other hand, different testing set-ups have a considerable effect on the resultant tensile behavior, hampering the comparison among the experimental results. In general, the FRCM coupons are rectangular or dumbbell-shaped, which can be cast by mortar with one or more layers of fiber grids. The connection between the specimen and the testing machine needs to ensure efficient transmission of tension while at the same time avoiding twisting and eccentricity as much as possible. The two currently used gripping methods are the clevis grip and the clamping grip. The specific gripping technologies and their effect on the experimental results will be reviewed in detail in the next section. It should be mentioned that many researchers have now acknowledged this effect, both from an experimental phenomenological [11,17,18,23] and theoretical [24–26] point of view, because it has been observed that failure modes triggered are very dependent on the specimen configurations and the clamping system used. Although the fiber fracture that may occur in the tensile test hardly ever occurs in actual engineering applications, the tensile tests are of some significance and do reflect the degree of the bond between mortar and fiber textile to some extent, since interfacial slip is a commonly observed failure mechanism in coupon tests regardless of the experimental setup. For instance, in the coupon test, there's an inelastic slippage between dry fiber and matrix, and the analytical model proposed can indirectly be used to calibrate the mechanical properties (in terms of shear stress, slip) of the interface.

In such a context, it is therefore interesting to develop analytical models for describing the non-linear behavior of FRCM coupons subjected to tension tests, because fast and stable computational results can be useful to both simulate reinforced structures in absence of extensive preliminary characterizations (rarely available), and also provide possible theoretical perspectives on the interpretation of complex experimental phenomena. Although there are differences in the boundary (loading) conditions, the constitutive relationships of the components, and the description of the mortar cracking process, the existing models are similar in terms of establishing simplified mathematical models and deriving the governing equations. In the analytical model proposed by Grande et al. [26], the brittle failure of the mortar and the softening behavior of the interface have been considered separately, while two patterns of cracks starting from the center and the end of the specimen have been discussed. In the model proposed by Minafò et al. [27], mortar and fiber are assumed elastic-brittle, while the failure of the interface is not involved. Furthermore, with the calibration of the interface shear stiffness through massive experimental data, the results for multi-layer reinforcements are also presented. The model by Focacci et al. [25] is devoted to the analysis of clevis grip tensile tests, where the softening behavior of both mortar and interface are considered; the force-displacement branches between the occurrence of successive cracks are reproduced by the increase of the cracking width. On the other hand, it cannot be denied that refined numerical models are also attractive to investigate the sensitivity of the outcomes in presence of more complex constitutive models and different boundary conditions [8,28,29], or to reflect the inhomogeneity of the material properties [30] as well as the presence of initial defects of the specimens [31]. Instead of adopting sophisticated analytical and numerical models, another option is to resort to the Aveston-Cooper-Kelly (ACK) model originally developed to describe the tensile stress-strain behavior of brittle matrix composites [32], or similar simplified approaches as discussed in Ref. [33]. Such simple models are already relatively effective for predicting the tensile behavior of FRCM [8,33–35]. However, the approach proposed here can be still used to provide information with more insight into the local behavior of the interface between dry fiber and matrix. In this regard, the present procedure can be seen as an advancement in the knowledge about the damage processes developing in the different components of the reinforcing system that allows obtaining a much more reliable prediction of the expected efficacy in a strengthening intervention.

Facing the complex damage modes exhibited by an FRCM composite under tension, their theoretical and computational prediction -which involves the damage of the interface between mortar and fiber textile as well as that of the mortar layers-is not an easy task and to some extent an open issue. This issue has been only partially tackled in the aforementioned models [25–27], which are based on different strategies to solve simplified governing equations. First, the sequence in which each component (mortar, fiber textile, and interface between them) enters in the inelastic stage is difficult to determine in advance; second, it is tricky to establish how the components behave after the local damage of one of them.

In such an intricate framework, the present paper proposes and discusses an analytical model for describing the non-linear behavior of FRCM coupons subjected to tension (under a clamping grip hypothesis) that can take into account the failure of all components, and provides a procedure based on closed-form solutions to determine along the entire length of the coupon stress and displacement field of each layer. The coupon is subdivided into three different layers: external mortar, internal fiber textile and an interface between mortar and fiber. The interface exchanges tangential stresses between mortar and fiber layers, which are assumed subjected to uniaxial tensile stresses. Under the hypothesis of elastic materials, writing the equilibrium and the constitutive equations for all the components, an ordinary differential equation (ODE) system is derived, which can be solved analytically provided that suitable boundary conditions are imposed. If it is assumed that mortar can concentrate damages on localized cracks and that the interface exhibits an elastic-perfectly brittle behavior with residual tangential strength, the ODE system still admits analytical solutions, which deserve to be discussed with the aim of predicting the local state of damage of the coupon at any value of the externally applied load, as well as to have an insight into the global behavior beyond the elastic limit. Three cases are discussed: in the first one it is assumed that cracks appear in the mortar layer and the interface remains elastic (Case 1), in the second one that the interface behaves inelastically and mortar elastically (Case 2), and in the third one that both mortar layer and interface exceed the elastic limit (Case 3). A comprehensive comparison with available experimental stress-strain curves obtained on a sufficiently large dataset of coupons tested in uniaxial tension is provided to show the reliability of the approach proposed. Thanks to its rapidity and stability, the influence of some mechanical parameters such as elastic slip limit of the interface, residual strength of the interface and mortar tensile strength is evaluated, and interesting deductions are made on the failure modes triggering and the local state of stress of all the components.

2. The analytical model

2.1. Review of experimental results

The experimental results available show that the typical tensile behavior of an FRCM coupon is trilinear: The first stage is elastic before the appearance of cracks in mortar layers; in such a phase the coupon stiffness is dependent on elastic and geometric properties of all the components. The second stage is characterized by the appearance of more cracks, sometimes an evident slippage at the interface occurs and multiple oscillations and experimental instabilities of the global stress-strain curve are visible, whose stiffness is significantly reduced. The third stage is characterized by a stabilization of the crack pattern, where no new cracks are formed, but only the expansion of the already formed ones occurs. The stiffness at this stage progressively becomes -in

agreement with intuition-almost equal to the stiffness of the fiber textile due to the extensive failure of the bond between the mortar and the textile. The existing experimental database available in the literature -which is quite large-gave an opportunity to calibrate the aforementioned trilinear tension stiffening model, see for instance Ref. [35]. According to a relatively wide set of experimental observations, three types of failure modes are generally categorized [16–19]. Type A is a failure at the clamps; Type B is characterized by matrix cracking with eventual fibers rupture; Type C is a matrix cracking coupled with fibers slippage at the clamps. As mentioned earlier, the failure modes can be quite dependent on the experimental setups, the typical trilinear behavior can only be observed when no premature failure at the ends occurs so that the full tensile load-bearing potential of the composite can be developed.

In order to assign the boundary conditions of the model reasonably, it's crucial to determine the conditions at the loading edge of the specimen during the tensile test. To transfer the external load from the loading machine to the specimen, one way is to directly pass the tensile stress through specific devices, such as employing a metal plate buried inside the specimen, or an alternative is to proceed by a flange fixed at the end of the dumbbell-shaped test piece (protected by rubber) [10,23]. Another way is to apply perpendicular pressure at the end of the coupon: the testing machine can directly clamp the end with a reinforced tab (referred as clamping grip here) [3,6–8,11], or it is possible to stick metal plates on both sides at the end of the specimen, so that the testing machine can apply tension to the shackle that connects the two plates (usually known as clevis grip) [9,12–15]. The clevis gripping method recommended by the ACI standard usually leads to end slippage, resulting in an underestimation of the tensile strength of the FRCM coupon, with the third stage of the coupon constitutive law not being observed [18,23]. Moreover, the strength of the specimen turns out largely influenced by the length of the plate at the end. Therefore, many researchers have recommended the clamping grip for achieving a full mechanical characterization of the FRCM system by avoiding premature mortar failure and textile slippage at the end [17,19]. However, it is undeniable that the clevis test can also allow observing the fiber-matrix bond effect, so some scholars believe that it is essentially a fiber–matrix bond test rather than a characterization test of the tensile properties [24,25]. In this paper, the study is mainly limited to the clamping gripping method, and readers interested in a theoretical model specifically developed for the clevis setup are referred to a recent study by Focacci et al. [25].

In this paper, to provide the necessary validation of the analytical model, the experimental campaign conducted by Carozzi et al. [3] is used. Rectangular PBO-FRCM coupons were tested according to the ACI standard, but with the clamping grip system; in addition, the ends were treated with sandblasting and reinforced by epoxy resin, as shown in Fig. 1-a. The geometrical and mechanical properties of the specimens belonging to the so-called PBO1-FRCM group (according to data and definitions provided in Ref. [3]) are summarized in Table 1; they represent the basic reference parameters for the great part of the calculations carried out in the present paper. The experimental campaign could not provide a direct method to determine the interface stress-slip relationship; however, this parameter can be provided by pull-out tests, as carried out in some other studies focusing on the mortar-fiber interface relationship [36–38]. In this study, according to previous literature available analyzing the same tests [30], for the shear strength, a value of about 75% of the mortar tensile strength is assumed, with a slip at the elastic limit equal to 0.015 mm as shown in Table 2.

Considering a clamping grip set-up, it is difficult to determine the stress and displacement inside the loading device with a simple analytical strategy, but it seems reasonable to hypothesize, as schematized passing from Fig. 1-a to Fig. 1-b, that the formation of the first cracks occurs near the loaded edges. In what follows, to simplify the model, the loading devices are not considered (because a specific model would be necessary) and we assume that the earliest cracks appear in mortar layers at both ends of the specimen ($x = \pm L/2$) excluded the devices and that the interface still behaves elastically after the formation

Table 1
Parameters adopted for the analytical models.

Component	Parameter	Symbol and unit	Value
Mortar	Young's modulus	E_m [MPa]	6000
	thickness (one layer)	t_m [mm]	5
	tensile strength	f_{tm} [MPa]	3.65
	compressive strength	f_{cm} [MPa]	>15
Fiber textile	Young's modulus	E_f [MPa]	215900
	equivalent thickness	t_f [mm]	0.046
	length	L [mm]	280
	width	B [mm]	40
	tensile strength	f_{tf} [MPa]	3397

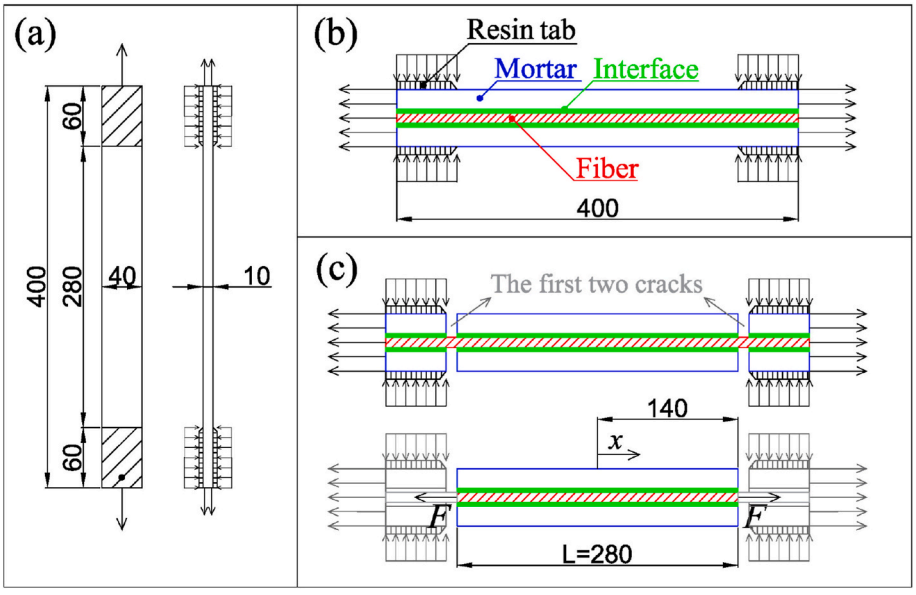

Fig. 1. Scheme adopted for the tensile test set-up on FRCM coupon (a), and the corresponding model before initial cracking at both ends (b), and during the whole loading process after initial cracks (c). (Measures in the figure is mm).

Table 2
Interface parameters adopted for Case 1 and Case 2.

Parameter	Symbol and unit	Value	
		Case 1	Case 2
shear strength	τ_m [*MPa*]	/	2.5
stiffness	K_i [N/mm^3]	166.67	166.67
elastic slip limit	s_e [*mm*]	/	0.015
residual strength	τ_r [*MPa*]	/	0/0.125/0.25

of the cracks (as it will be discussed in Section 3.1). Thus, all subsequent analyses can follow the simplified mathematical model depicted in Fig. 1-c, where mortar exhibits normal stresses equal to zero at the extremes.

2.2. Analytical model and ODE system

The analytical model is expected to describe the typical non-linear behavior of an FRCM coupon under tension, meaning that with the fiber elongation, transversal cracks gradually develop in the mortar layer and the interface can slip, until the bond is no longer effective, and the fiber strip alone bears the tensile forces applied at the vertical edges. Based on the experimental phenomena, a classic simplified mathematical model is proposed, see Fig. 2, which relies upon considering three different components working in parallel: the mortar layers (placed symmetrically), the fiber textile, and a zero-thickness interface between them, which has the role to transfer the load from the fiber to mortar and vice-versa, through a suitable tangential stress-slip law. Consistent geometric dimensions and uniform distribution of the materials are assumed along the width, length and thickness of the coupon. Under the above ideal assumptions, it is not difficult to deduce that an FRCM coupon subjected to tension exhibits double symmetry: one symmetry axis is horizontal and coincides with the fiber textile centroid and the other is vertical and placed at equal distance from the loading devices applied at the extremes of the specimen.

Therefore, the analyses can be carried out considering only one quarter of the coupon as shown in the enlarged area in Fig. 2-a. The independent variables considered are the following: the horizontal displacement fields of mortar and fiber (u_m and u_f) and the normal stress acting on the aforementioned two layers (σ_m and σ_f), respectively. The displacements of both mortar and fiber in correspondence with the centroid of the coupon (where the origin of the frame of reference is located) are equal to zero, so that rollers with horizontal axis are placed on the vertical symmetry axis. The *x*-axis is set horizontally along the length of the fiber for the sake of convenience, with orientation from the left to the right. The *y*-axis runs vertically along the thickness of the coupon, with upwards orientations, as depicted in Fig. 2-a. The parameter t_m indicates the mortar layer thickness and t_f the semi-thickness of the fiber textile.

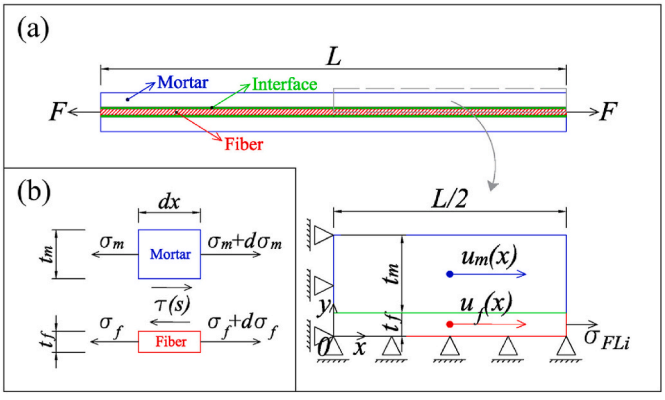

Fig. 2. Analytical model adopted for an FRCM coupon subjected to tension (a) and stress analysis for the infinitesimal parts (b).

Taking into consideration a portion of the coupon with infinitesimal length equal to *dx* as shown in Fig. 2-b, the equilibrium conditions between mortar and fiber layers can be written as follows:

$$\begin{cases} t_f \dfrac{d\sigma_f}{dx} = \tau(s) \\ t_m \dfrac{d\sigma_m}{dx} = -\tau(s) \end{cases} \tag{1}$$

The shear stress acting at the mortar-fiber interface is denoted with $\tau(s)$. An elastic-perfectly brittle behavior with residual tangential strength (bi-linear behavior) is assumed:

$$\begin{cases} \tau = K_i \quad s \quad (s \le s_e) \\ \tau = \tau_r \quad (s > s_e) \end{cases} \tag{2}$$

Where the slip *s* denotes the difference of the horizontal displacements of fiber and mortar:

$$s = u_f - u_m \tag{3}$$

In the previous equations K_i indicates the elastic stiffness assumed for the interface, τ_r is the residual shear strength and $s_e = \tau_m / K_i$ is the elastic limit of the interface slip, τ_m indicating the peak strength reached at the elastic limit.

The constitutive relationships of the two materials in the elastic range allow writing the following equations:

$$\begin{cases} \sigma_f = E_f \dfrac{du_f}{dx} \\ \sigma_m = E_m \dfrac{du_m}{dx} \end{cases} \tag{4}$$

Where E_m and E_f are the elastic moduli of mortar and fiber layers, respectively. An ODE system can be deduced by combining Eq. (4) and Eq. (1), then analytically solved with the imposition of suitable boundary conditions at different instants of the loading process, as explained in detail in the following sections.

With the aim of realistically reproducing the expected behavior of an FRCM coupon under tension, considering the high tensile strength of the fiber textile in comparison with that of the mortar layers, as well as the experimentally observed failure mechanism, fiber rupture may be considered as the instant where the failure of the entire coupon is reached. It can be also assumed that the fiber textile behaves elastically during the whole experiment. The following three different cases may occur, depending on the mutual mechanical properties of mortar and interface:

Case 1: the interface behaves elastically, and the mortar layer cracks, meaning that only a non-linear behavior for mortar is considered. Cracks are assumed concentrated, and mortar behaves elastically almost everywhere, exception made for those points where cracks are located. Two sub-cases are discussed, the first assuming an elastic-perfectly brittle behavior for mortar, the second imposing that the crack opening is ruled by a certain fracture energy, i.e. that there is an analytical relationship between crack width and the stress acting in correspondence of the crack.
Case 2: the interface behaves non-linearly, but the tensile strength of mortar is assumed very high and it remains in the elastic phase, meaning that only the non-linear behavior of the interface is considered.
Case 3: interface and mortar layer exhibit non-linearity contemporarily; in this latter case, both mortar cracking and interface slippage are observed.

For Case 1, it is assumed that mortar forms concentrated cracks in particular positions of the coupon along its length. Therefore, its

behavior between two contiguous cracks is elastic and an analytical solution can be easily deduced by progressively changing the boundary conditions and the length of the portion of coupon considered. In other words, the same analytical model can be adopted for different intact mortar portions. Let us first consider the intact coupon at the beginning of the test (after the appearance of initial cracks at the two extremes) and let us focus on one quarter of it for double symmetry reasons (shaded area in Fig. 3). With reference to Fig. 3, along the x-axis, the normal stress in the mortar layer is zero at the free edge located on the right and is expected to attain the maximum in correspondence of the origin O, since non-null tangential stresses -generated by the slip between matrix and underlying fiber textile-arise at the interface between matrix and fiber. Thus, the crack will appear in the middle of the coupon. Let us label such analysis step as $i = 1$; nothing changes considering other steps, making sure to change the length of the portion of coupon (always half the length in the previous step), it is possible to identify two meaningful instants to deduce step by step the global load-displacement behavior of an FRCM coupon under tension:

1) Instant A: It represents the instant when mortar on the vertical symmetry axis reaches the maximum tensile strength, as shown in the schematic diagrams on the left in Fig. 3;
2) Instant B: It is the instant immediately after the formation of the crack in Instant A, as shown by the right-hand diagrams of Fig. 3.

Proceeding step by step, the length of the coupon analyzed reduces by a factor 1/2. To correctly identify the displacement at the loaded edge, suitable boundary conditions must be assumed on the displacements to assign on the left edge of the portion of the coupon considered, making use of the results obtained for the contiguous portion of the coupon and calculated in correspondence of the right edge (which is regarded as the left edge for the coupon portion under consideration).

After the first crack occurs, the mortar layer cracks and divides into two geometrically identical parts on both sides of the crack, allowing to perform the same analysis carried out in the previous step. Following this simple procedure, the behavior of an FRCM coupon under tension can be described during the whole loading process, even in the inelastic range, because cracks will continue to appear in pre-assigned positions of the mortar layer until the fiber rupture.

Case 2 may occur in practice when the coupon length is too small, so that mortar cannot attain its maximum strength, or typically when the interface strength is too small if compared with that of the mortar. Such behavior has been observed by many researchers in the experiments, and denoted with the term 'saturation crack spacing' [39]. Phenomenologically, the saturation crack spacing indicates a distance between two contiguous cracks appearing in mortar layers that is too small to allow the formation of further cracks, which promotes at the same time the activation of the interface non-linearity.

To summarize, Table 3 and Fig. 4 show respectively a synopsis of the cases considered and the corresponding constitutive models adopted. In Case 1, as already mentioned, two mortar models (labeled as Case 1-a and Case 1-b) are adopted under the hypothesis of elastic behavior for the interface. In Case 2, different values of residual strength are considered in order to show the role played by such parameter on the local and global response, maintaining the mortar layer elastic. Finally, Case 3 combines mortar cracking and inelastic behavior of the interface. For all models, as already mentioned, the failure of the coupon is controlled by the rupture of the fiber, which is characterized by an elastic behavior throughout the whole analysis.

3. Case 1: mortar failure

3.1. Case 1-a: Elastic-perfectly brittle mortar with elastic interface

In this case, we assume that the mortar matrix behaves in an elastic-perfectly brittle manner, whereas the interface is assumed elastic. Combining Eq. (4) and Eq. (1), and re-arranging the equations isolating on the left the first derivative of the independent variables, the following ODE system can be obtained:

Table 3
Constitutive models for the different cases discussed.

Cases	Mortar	Interface	Fiber
Case1-a	Elastic-brittle	Elastic	Elastic-brittle
Case1-b	Elastic-softening		
Case2	Elastic	Elastic-brittle with/without residual strength	
Case3	Elastic-brittle	Elastic-brittle with residual strength	

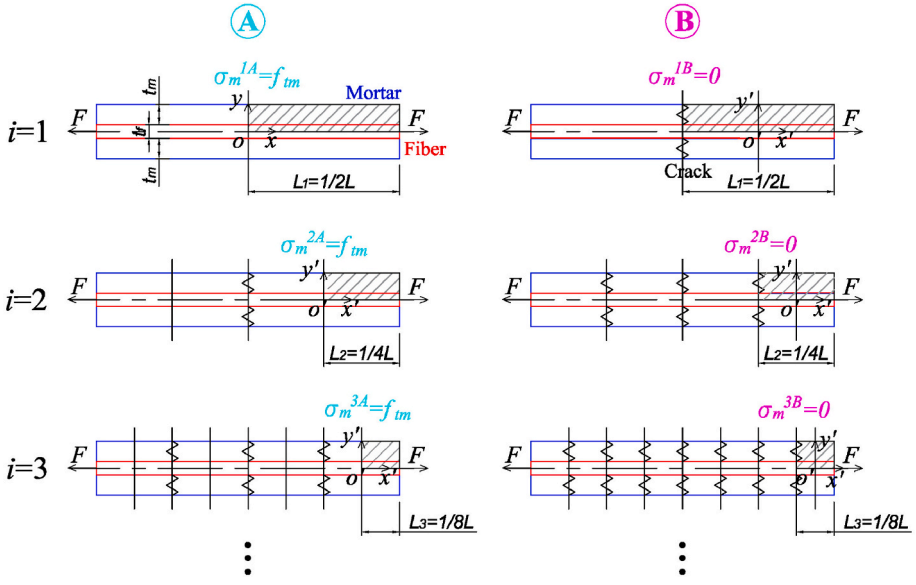

Fig. 3. Scheme of the analytical calculations carried out for Case 1 with formation of concentrated cracks inside mortar (the shaded area is the portion of the coupon considered in the analyses).

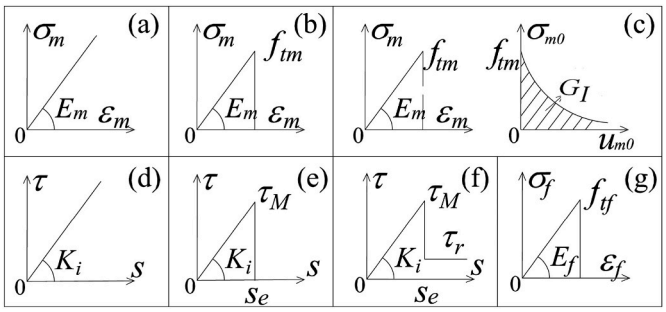

Fig. 4. Constitutive models assumed for the different components: (a) Elastic mortar, (b) Elastic-perfectly brittle mortar, (c) Elastic-softening mortar, (d) Elastic interface, (e) Elastic-brittle interface without residual strength, (f) Elastic-brittle interface with residual strength and (g) Elastic-perfectly brittle fiber textile.

$$\begin{bmatrix} \frac{du_f}{dx} \\ \frac{d\sigma_f}{dx} \\ \frac{du_m}{dx} \\ \frac{d\sigma_m}{dx} \end{bmatrix} = \begin{bmatrix} 0 & \frac{1}{E_f} & 0 & 0 \\ \frac{K_i}{t_f} & 0 & -\frac{K_i}{t_f} & 0 \\ 0 & 0 & 0 & \frac{1}{E_m} \\ -\frac{K_i}{t_m} & 0 & \frac{K_i}{t_m} & 0 \end{bmatrix} \begin{bmatrix} u_f \\ \sigma_f \\ u_m \\ \sigma_m \end{bmatrix} \tag{5}$$

The general solution for such an ODE system can be trivially obtained as follows:

$$\begin{bmatrix} u_f \\ \sigma_f \\ u_m \\ \sigma_m \end{bmatrix} = C_1 \begin{bmatrix} 1 \\ 0 \\ 1 \\ 0 \end{bmatrix} + C_2 \left(\begin{bmatrix} 1 \\ 0 \\ 1 \\ 0 \end{bmatrix} x + \begin{bmatrix} 0 \\ E_f \\ 0 \\ E_m \end{bmatrix} \right) + C_3 \begin{bmatrix} -t_m\alpha \\ -t_m/t_f \\ t_m\beta \\ 1 \end{bmatrix} e^{\lambda_3 x} + C_4 \begin{bmatrix} t_m\alpha \\ -t_m/t_f \\ -t_m\beta \\ 1 \end{bmatrix} e^{\lambda_4 x} \tag{6}$$

in which $C_{1,\dots,4}$ are integration constants and coefficients λ_3, λ_4, α and β are the following:

$$\begin{cases} \lambda_3 = \sqrt{K_i \left(\frac{1}{E_m t_m} + \frac{1}{E_f t_f} \right)} \\ \lambda_4 = -\sqrt{K_i \left(\frac{1}{E_m t_m} + \frac{1}{E_f t_f} \right)} \\ \alpha = \sqrt{\frac{E_m t_m}{E_f t_f K_i \left(E_f t_f + E_m t_m \right)}} \\ \beta = \sqrt{\frac{E_f t_f}{E_m t_m K_i \left(E_f t_f + E_m t_m \right)}} \end{cases} \tag{7}$$

It is interesting to point out that constants $C_{1,\dots,4}$ have the following units of measure: C_1 in mm, C_2 is a pure number, C_3 and C_4 in MPa. Constants $\lambda_{3,4}$ are in mm and α, β in 1/MPa. To determine the constants of integration, the following procedure is applied for the Instant i-A. At the i-th Instant, we can imagine that the coupon is constituted by $n_{sc,i} = 2^{(i-1)}$ sub-coupons (abbreviated with '*sc*' at the subscript) of length $2L_i$ placed in series, with $L_i = L/2^i$. Isolating the $n_{sc,i}$ -th coupon and analyzing it separately without considering the rigid horizontal translations induced by the fact that sub-coupons are connected to neighboring ones (in other words the ODE solution is applied on a coupon with length $L/2^i$), the boundary conditions to apply to all sub-coupons are the following:

$$\begin{cases} u_f\big|_{x=0} = 0 \\ u_m\big|_{x=0} = 0 \\ \sigma_m\big|_{x=0} = f_{tm} \\ \sigma_m\big|_{x=L_i} = 0 \end{cases} \tag{8}$$

Indicating respectively with $u_{fLi}^{iA,j}$ and $\sigma_{fLi}^{iA,j}$ the displacement and the stress in the fiber textile of the j-th sub-coupon along L_i, for Instant i-A, such quantities can be calculated by finding $C_{1,\dots,4}$ in Eq. (6) through the imposition of boundary conditions, Eq. (8). Then, the loaded edge displacement and stress are the following:

$$\begin{cases} u_{fLi}^{iA} = n_{sc,i} u_{fLi}^{iA,j} \\ \sigma_{fLi}^{iA} = \sigma_{fLi}^{iA,j} \end{cases} \tag{9}$$

Assuming an elastic-perfectly brittle constitutive relationship for mortar (Case 1-a), in the mortar section attaining its tensile strength, the normal stress immediately drops to zero and Instant i-B occurs immediately after Instant i-A, making the assumption that the displacement at the loaded edge is maintained unaltered. The previously mentioned condition about the unaltered displacement of the fiber at the loaded edge requires that the fiber displacement of the right loaded edge of the sub-coupon j is $u_{fLi}^{iA,j}$. Therefore, the boundary conditions to apply at Instant i-B are the following:

$$\begin{cases} u_f\big|_{x=0} = 0 \\ u_f\big|_{x=L_i} = u_{fLi}^{iA,j} \\ \sigma_m\big|_{x=0} = 0 \\ \sigma_m\big|_{x=L_i} = 0 \end{cases} \tag{10}$$

Indicating respectively with $u_{fLi}^{iB,j}$ and $\sigma_{fLi}^{iB,j}$ the displacement and the stress in the fiber textile of the sub-coupon *j* along L_i, for Instant i-B, such quantities can be again calculated finding $C_{1,\dots,4}$ in Eq. (6) through the imposition of boundary conditions, Eq. (10). Then, the loaded edge displacement and stress are the following:

$$\begin{cases} u_{fLi}^{iB} = n_{sc,i} u_{fLi}^{iB,j} \\ \sigma_{fLi}^{iB} = \sigma_{fLi}^{iB,j} \end{cases} \tag{11}$$

The geometric distribution of cracks in Instant i-B can then be utilized in Instant (i+1)-A, following the above-described procedure, the coupon behavior until the fiber fracture can be obtained. The stresses and interface slip distributions along half of the coupon length are presented in Fig. 5. Instants A (solid lines) and B (dashed lines) before and after the occurrence of each crack are indicated by different colors. Six Instants are depicted for the sake of clearness as well. The symmetric crack pattern and the same stress distributions in each uncracked mortar portion (i.e. inside a sub-coupon) are clearly visible. The stress-strain global behavior is shown with a black solid line in Fig. 6, where the strain is obtained by dividing the displacement at the loaded end by the full length of the coupon. Six teeth corresponding to the cracking sequence can be identified. It is also important to point out that such a very simple model is continuing to develop cracks in the third stage (the sixth crack), approximating it with a sawtooth behavior. Such a peculiar outcome, not fully consistent with experiments, is a consequence of the elastic assumption of the interface, leading to the situation that the interface still can provide enough shear stress to allow mortar failure even on a very short portion of the coupon.

3.2. Case 1-b: Elastic-softening mortar with elastic interface

In Case1-b, it is assumed that after the mortar reaches its maximum strength (Instant A), the mortar stress does not drop instantaneously to zero, because the mortar is assumed brittle with softening ruled by a certain fracture energy as shown in Fig. 4-c.

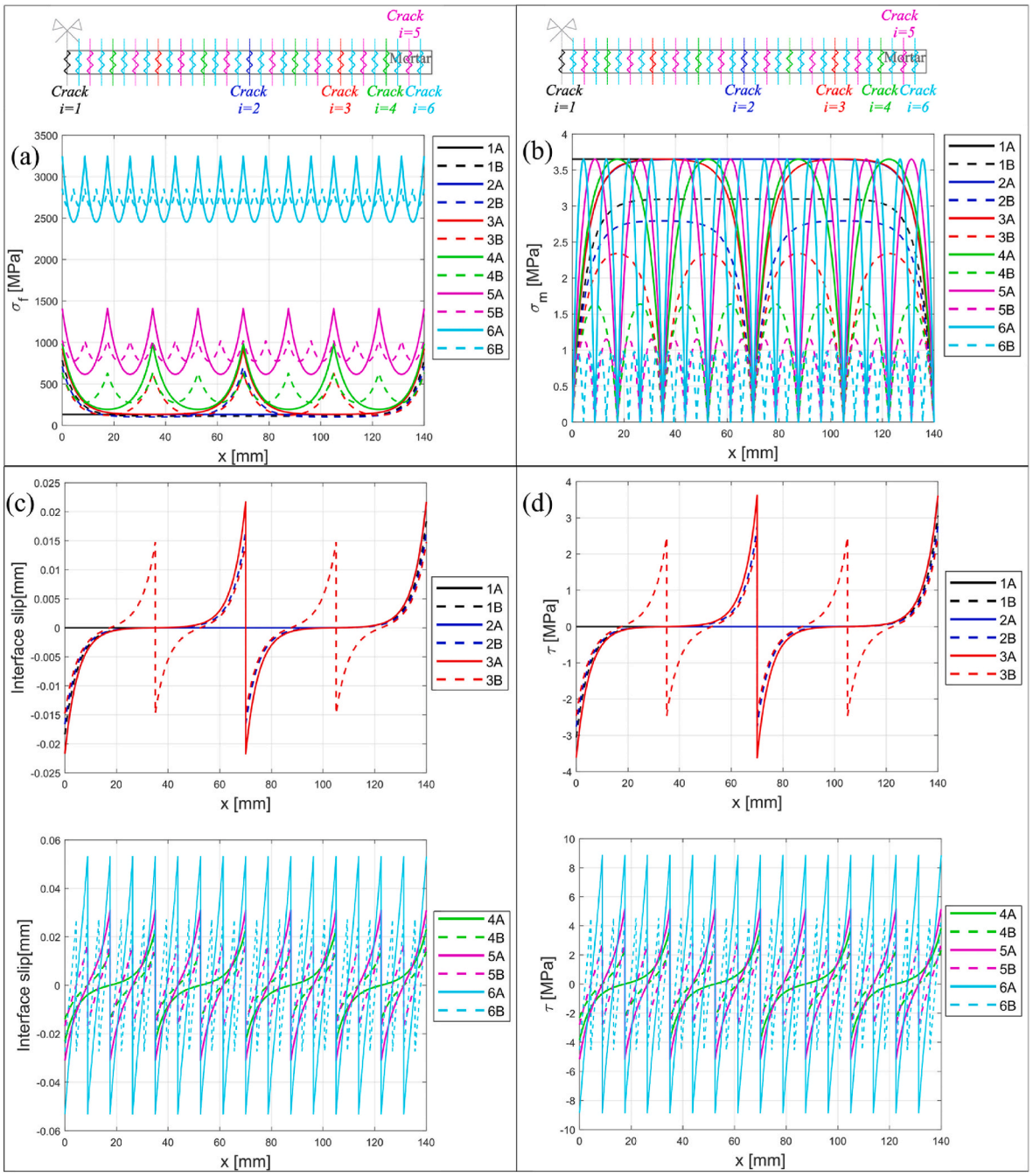

Fig. 5. Case 1: Distribution of (a) fiber tensile stress, (b) mortar tensile stress, (c) interface slip and (d) interface shear stress until fiber rupture.

The crack width increases progressively, allowing to see a snap-back of the global curve until the crack can be considered fully developed (Instant B). The following exponential relationship between mortar tensile stress and mortar displacement (which represents the concentrated crack width) at the local origin of the sub-coupon (i.e. where mortar attains the maximum stress) is assumed:

$$\sigma_m|_{x=0} = f_{tm} e^{\frac{-f_{tm}}{G_I} u_m|_{x=0}} \tag{12}$$

in which the fracture energy G_I is the shaded area depicted in Fig. 4-c, and enclosed between the mortar stress-displacement (crack width) relationship, Eq. (12), and the horizontal axis. The description of the softening behavior of mortar under tension by means of exponential functions is a classical numerical strategy that can be found both in recent [24,40] and dated literature [41]. Such numerical assumption is grounded on a wide set of experimentations devoted to the topic, see for instance Ref. [42]. On the other hand, no matter the specific law assumed in the tensile inelastic stage for mortar is; in fact, any analytical function can be adopted (such as the classical linear relationship) for the model without additional numerical issues.

The solutions for Instants i-A are exactly the same deduced in Case 1-a. However, in Case 1-b it is also possible to reproduce what happens between Instants A and B, simply solving the same ODE system, under the imposition of different boundary conditions. If in $x = 0$, the stress is σ_{m0}, with $0 \leq \sigma_{m0} \leq f_{tm}$, then at an intermediate instant between Instants A and B, we have:

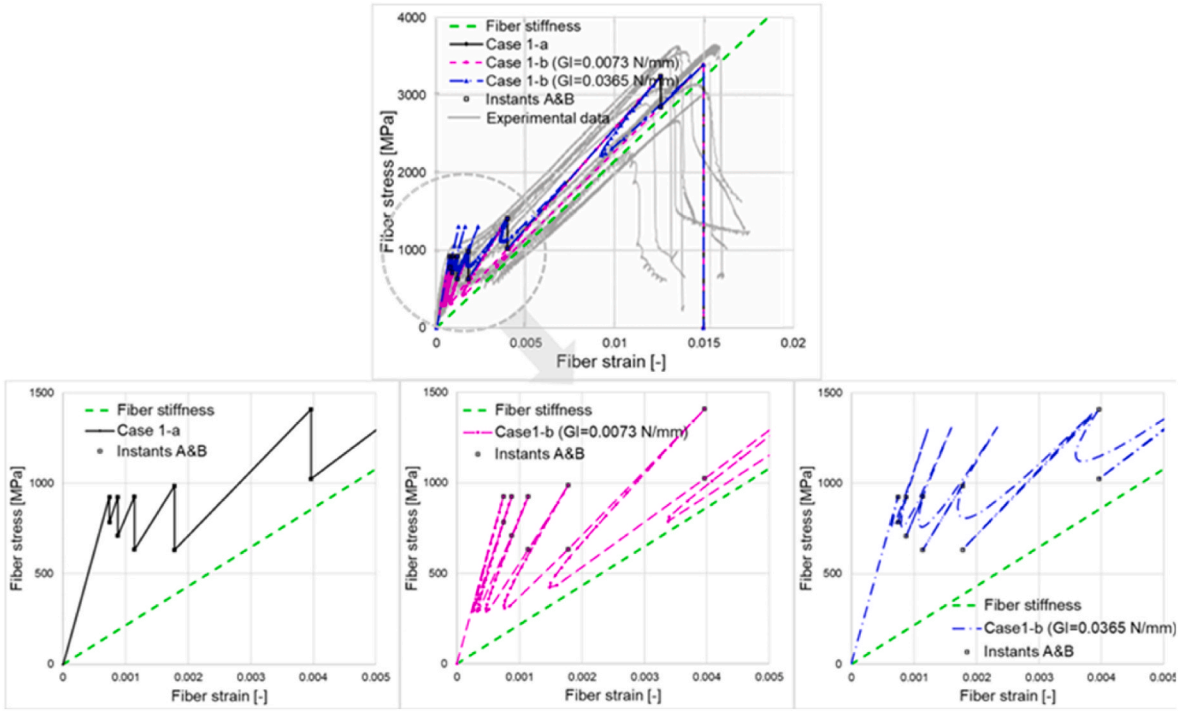

Fig. 6. Global stress-strain relationships obtained in Case 1-a and Case 1-b and comparison with experimental data.

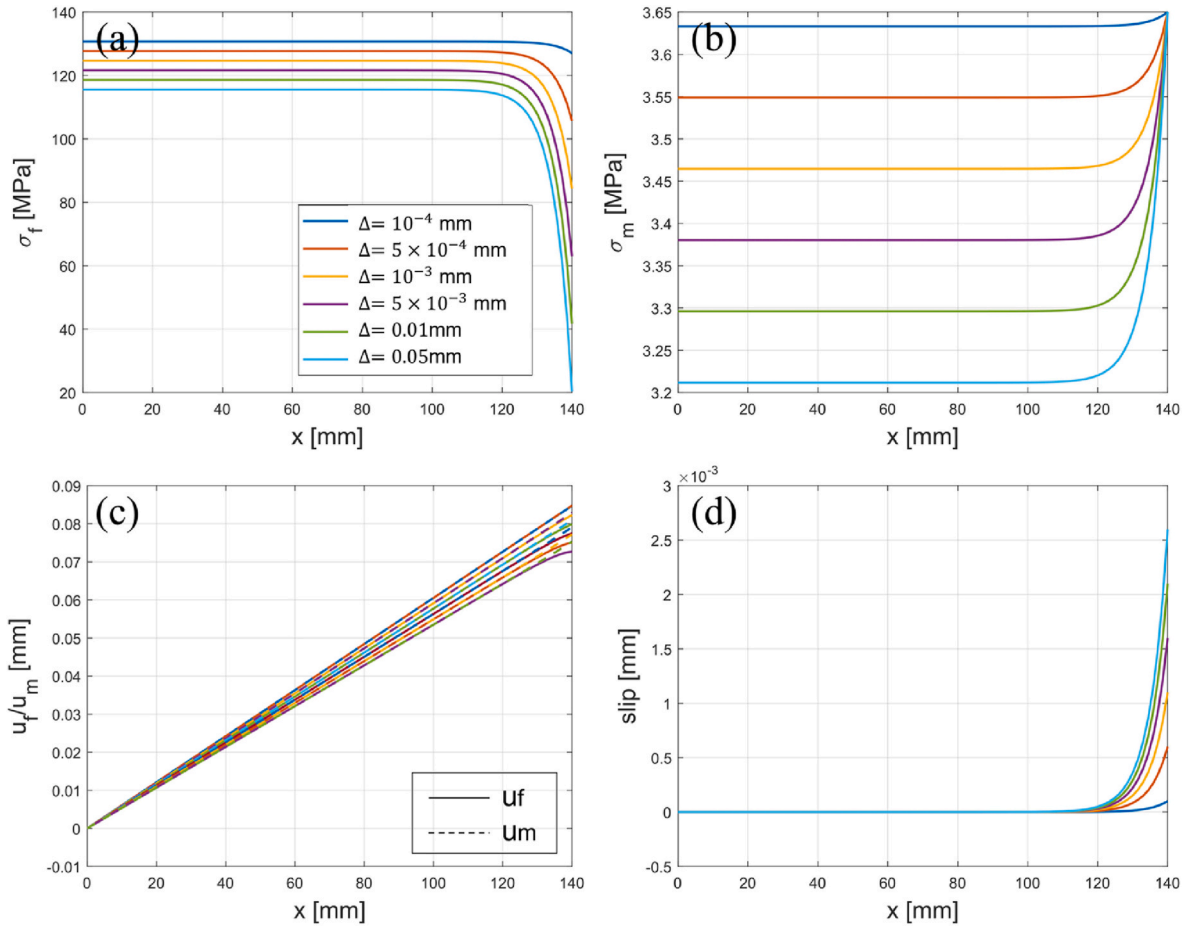

Fig. 7. Distributions of (a) fiber stress, (b) mortar stress, (c) fiber and mortar displacements, and (d) interface slip at increasing displacement Δ applied at the loaded edge. Δ is increased to evaluate the instant when the initial cracks appear at clamping ends.

$$\begin{cases} \sigma_m|_{x=0} = \sigma_{m0} \\ u_m|_{x=0} = \dfrac{G_I}{f_{tm}} ln\left(\dfrac{f_{tm}}{\sigma_{m0}}\right) \\ u_f|_{x=0} = 0 \\ \sigma_m|_{x=Li} = 0 \end{cases} \tag{13}$$

The global stress-strain relationships of the coupon obtained with different values of G_I are plotted in Fig. 6. It can be seen that Instants B are the same for both cases, since they represent a snapshot of the mechanical system at the same displacement of the fiber at the loaded edge. The much evident difference is the branch within Instants A and B: in Case1-a, it is indeed imposed to drop down the force applied to maintain the same displacement; in Case1-b a snap-back can be reproduced, which appears very pronounced for small values of the fracture energy. If, on the contrary, G_I is sufficiently large, the typical oscillating behavior of the trilinear curve in stage 2 (and frequently observed experimentally) can be reproduced also numerically in a quite accurate way.

3.3. The model before the appearance of the first crack at the loaded edge

When we consider the model at the formation of the initial cracks near the loading devices (Fig. 1-b), the elastic ODE system of Eq. (5) still holds, and the boundary conditions that can be applied are the following:

$$\begin{cases} u_f|_{x=0} = 0 \\ u_m|_{x=0} = 0 \\ \sigma_m|_{x=L/2} = f_{tm} \\ (u_m - u_f)|_{x=L/2} = \Delta \end{cases} \tag{14}$$

The exact value of Δ (the slip between the mortar and fiber textile at the loaded edge) cannot be determined analytically in an easy way, but what is known is that the sign of Δ must be positive. A convenient strategy is to increase Δ until the possible peak normal stress at the origin in the mortar layer is reached. As can be seen in Fig. 7, the displacements of mortar and fiber are quite small along the whole coupon length, the interfacial slip is much smaller than the elastic limit, and the fiber stress is far from that responsible for the rupture of the fiber textile. Therefore, when simulating a real test made in the lab, it is reasonable to disregard such initial loading phase, i.e. that before the appearance of the initial two cracks at clamping ends, because this phase is limited at the early stages of the loading process and scarcely affects the subsequent analyses.

4. Case 2: failure of the interface

In this case, we assume that the interface behavior is bi-linear and discontinuous (elastic-perfectly brittle with residual strength), while mortar and fiber are elastic. No cracks can appear in the mortar, hence only one Instant, say A, needs to be re-defined, and there is a transition point where the interface behavior passes from elastic to inelastic. Let us indicate the abscissa of such a transition point with x_r (as shown in Fig. 8). x_r value needs to be decreased from L_i to 0; when $x_r = L_i$ the coupon has reached the elastic limit, whereas when $x_r = 0$ the interface is in the inelastic stage everywhere throughout the length of the specimen. When the stress in the fiber textile reaches the value assumed for the rupture of the yarns, the coupon fails and the analysis must be stopped.

The problem is split into two distinct regions, the first elastic and the second inelastic.

1) Elastic region

For the part where the interface behaves elastically ($0 \le x \le x_r$), the previously presented ODE system representing the field equations is still applicable, and can be solved with the boundary conditions below:

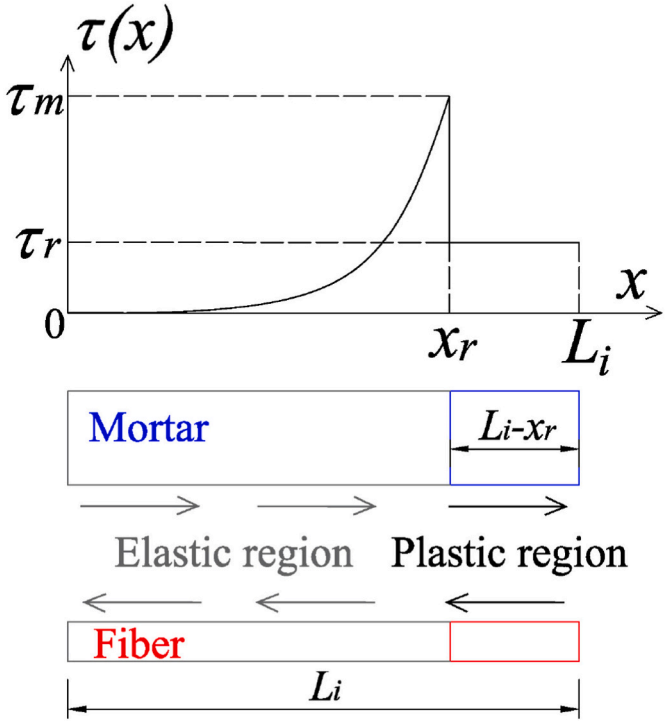

Fig. 8. Schematic diagram of the interface status in Case 2.

$$\begin{cases} u_f|_{x=0} = 0 \\ u_m|_{x=0} = 0 \\ (u_f - u_m)|_{x=x_r} = s_e \\ \sigma_m|_{x=x_r} = \dfrac{\tau_r(L_i - x_r)}{t_m} \end{cases} \tag{15}$$

2) Plastic region

The equilibrium equations for mortar and fiber textile in the inelastic part ($x_r < x \le L_i$) can be written as follows:

$$\begin{cases} \sigma_f = \sigma_f|_{x=x_r} + \dfrac{\tau_r(x - x_r)}{t_f} \\ \sigma_m = \dfrac{\tau_r(L_i - x)}{t_m} \end{cases} \tag{16}$$

The displacements at a certain abscissa x located in the inelastic part are the following:

$$\begin{cases} u_f = u_f|_{x=x_r} + \displaystyle\int_{x_r}^{x} \frac{\sigma_f}{E_f} dx \\ u_m = u_m|_{x=x_r} + \displaystyle\int_{x_r}^{x} \frac{\sigma_m}{E_m} dx \end{cases} \tag{17}$$

Integrating Eq. (17), it is possible to derive analytically such displacements as follows:

$$\begin{cases} u_f = u_f|_{x=x_r} + \dfrac{(x - x_r)}{E_f}\sigma_f\Big|_{x=x_r} + \dfrac{\tau_r(x - x_r)^2}{2E_f t_f} \\ u_m = u_m|_{x=x_r} + \dfrac{\tau_r}{E_m t_m}\left(L_i(x - x_r) - \dfrac{1}{2}(x - x_r)^2\right) \end{cases} \tag{18}$$

Remembering that the solutions at $x = x_r$ is already known from the elastic region, all quantities can be determined without the need to resort to complex computational methods.

To test the reliability of the approach, a sensitivity analysis is carried out with three different values of residual strength (0 MPa, $0.1\tau_m$ and $0.05\tau_m$), keeping the remaining quantities unchanged and equal to those reported in Table 2. Stresses and interface slip distributions along one-half of the coupon length are depicted in Fig. 9 at increasing values of the applied external load; whereas the global stress-strain curves are presented in Fig. 10. Obviously, when the residual friction of the interface is assumed to be equal to zero, the behavior of the coupon tends asymptotically to approximate that of the bare fiber textile when the inelastic region of the interface expands considerably. When the residual strength is not zero, the coupon stiffness is again equal to that of the dry fiber at large values of the applied load, but the deformability decreases by a value (which remains almost constant increasing the applied load) which is dependent on the amount of residual strength considered. In agreement with intuition, large values of such strength are associated with lower strains measured at the loaded edge of the dry fiber. It can be seen that a small portion of the interface is always in the elastic stage when the fiber rupture is reached, a feature that is consistent with the assumption that the relative slip at the origin is zero.

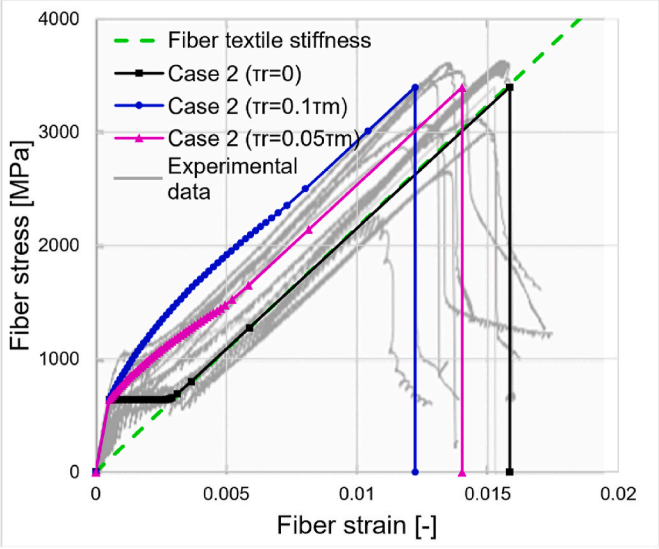

Fig. 10. Global stress-strain relationships obtained for Case 2 adopting different values of residual strength for the interface, and comparisons with experimental data.

5. Case 3: Simultaneous non-linear behavior of mortar and interface

5.1. The analytical approach

In this case, possible failures of all components are considered. Mortar is assumed elastic-perfectly brittle, while the interface is elastic-perfectly brittle with residual strength. Dealing with two components that could potentially behave inelastically, first of all, it is necessary to determine whether mortar and interface can simultaneously reach the inelastic states; if this is the case, the mortar layer can crack only after the interface has partially entered the plastic stage, otherwise, we fall

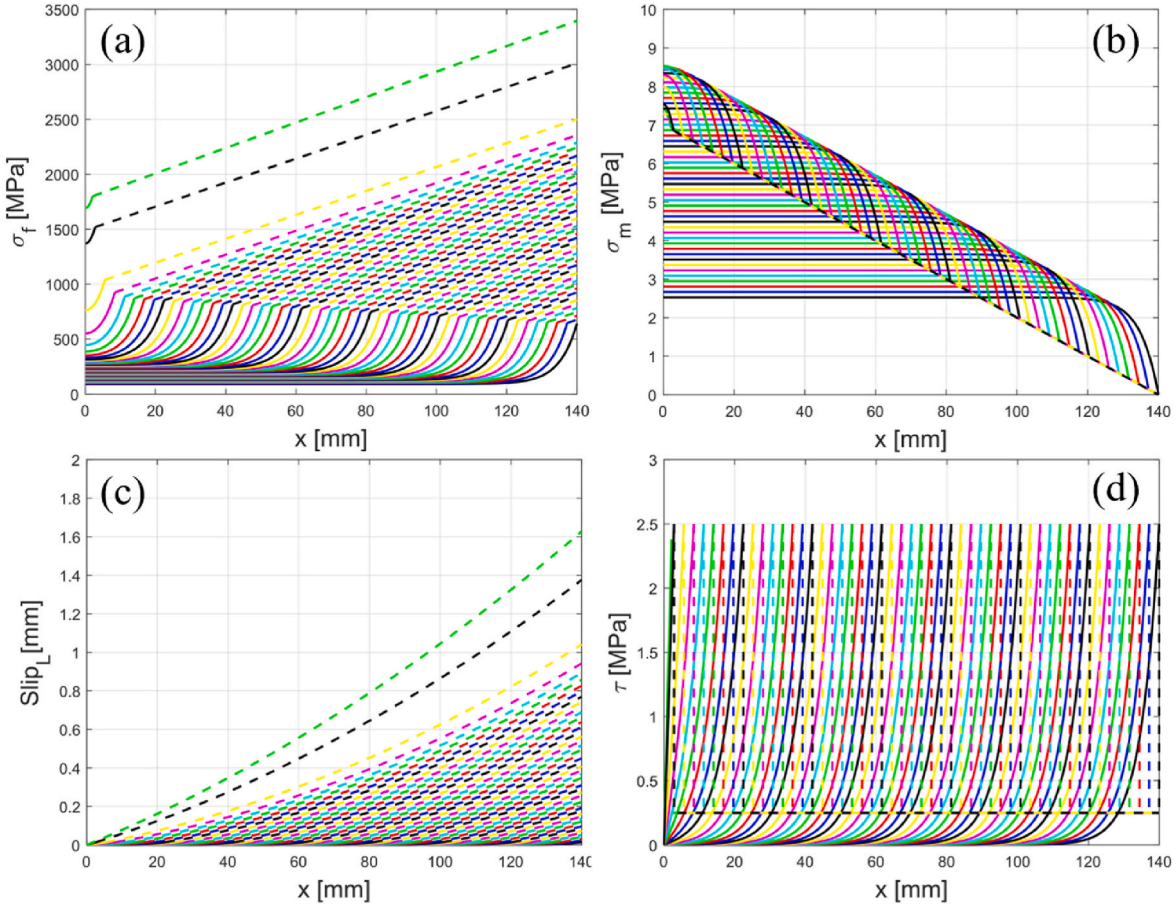

Fig. 9. Distribution of (a) fiber tensile stress, (b) mortar tensile stress, (c) interface slip, and (d) interface shear stress along half coupon length for Case 2 with $\tau_r = 0.1\tau_m$. The solid lines represent the elastic region, while the dashed lines the plastic region.

into Case 1, as extensively discussed in the previous Sections.

- Evaluation of interface inelastic behavior triggering

The fiber-mortar interface enters the inelastic stage when the maximum slip (which occurs at L_i) reaches the elastic limit s_e . Let us consider an intact portion of the mortar layer $2L_i$ long, Fig. 11-a, whose internal variables are calculated elastically because all the points inside such a portion are in the elastic phase by definition. According to the elastic results already discussed in Case 1, the interface slip at L_i can be deduced from the solution of the ODE in the elastic range, and utilizing boundary conditions to eliminate constants. More in detail, based on Eq. (6), it is possible to write separately the slips at $x = 0$ and $x = L_i$, as follows:

$$\begin{cases} s_0 = (u_f - u_m)|_{x=0} = (C_4 - C_3)(\alpha+\beta)t_m \\ s_{L_i} = (u_f - u_m)|_{x=L_i} = (C_4 e^{\lambda_4 L_i} - C_3 e^{\lambda_3 L_i})(\alpha+\beta)t_m \end{cases} \tag{19}$$

Remembering that at the origin $s_0 = 0$, it follows that $C_3 = C_4$, knowing from Eq. (7) that $(\alpha+\beta)$ cannot be equal to zero, because sum of two positive numbers. Also, from Eq. (7), it must be noted that $\lambda_4 = -\lambda_3$.

If a crack in the matrix layer occurs, which appears at $x = 0$, we can write other two boundary conditions at the left and right edges:

$$\begin{cases} \sigma_m|_{x=0} = C_2 E_m + C_3 + C_4 = f_{tm} \\ \sigma_m|_{x=L_i} = C_2 E_m + C_3 e^{\lambda_3 L_i} + C_4 e^{\lambda_4 L_i} = 0 \end{cases} \tag{20}$$

The above system of the equation provides the value of $C_3 = C_4$:

$$C_3 = C_4 = f_{tm} / \left(2 - e^{\lambda_3 L_i} - e^{-\lambda_3 L_i}\right) \tag{21}$$

Finally, we can write the slip at $x = L_i$ when a crack appears as follows:

$$s_{L_i} = \frac{t_m f_{tm}(\alpha+\beta)(e^{\lambda_3 L_i} - e^{-\lambda_3 L_i})}{(e^{\lambda_3 L_i} + e^{-\lambda_3 L_i} - 2)} = \frac{t_m f_{tm}(\alpha+\beta)}{tanh\left(\frac{\lambda_3 L_i}{2}\right)} \tag{22}$$

When $s_{L_i} > s_e$, then the interface has partially entered the inelastic stage at mortar cracking, and the solution for a part of the coupon is no longer elastic and needs to be recalculated.

On the other hand, to maintain the interface elastic everywhere until crack, meaning that we always have $s_{L_i} \le s_e$, the following inequality must hold:

$$tanh\left(\frac{\lambda_3 L_i}{2}\right) \ge \frac{t_m f_{tm}(\alpha+\beta)}{s_e} \tag{23}$$

Note that *tanh* (x) cannot be larger than one; if the right-hand side of the inequality is greater than one, there is no value of L_i that can satisfy Eq. (20), i.e., the interface will enter the plastic phase before any crack appears along the whole coupon. For example, if the material properties and the interface stiffness are kept constant, it can be seen that when s_e decreases, the value of the term on the right side of the inequality increases, in such a way that the right-hand side can become greater than one.

- Evaluation of mortar cracking

It is discussed here whether the mortar can crack after the interface has partially entered the plastic stage. First, it is necessary to determine the transition point between the elastic and inelastic stages along the interface (x_r). As observed in Case 2, the maximum mortar tensile stress (denoted here with σ_{m0}), is reached at the origin (centroid of the coupon); the value of σ_{m0} progressively increases and then decreases as the loading proceeds (Fig. 9-b). Analytically speaking, for any given x_r varying from Li to 0, for the elastic region, we can write the boundary conditions as in Eq. (15)., which combined with the solution of the ODE system, Eq. (6) and Eq. (7), allows deriving analytically σ_{m0} as follows:

$$\sigma_{m0} = \frac{\tau_r(L_i - x_r)}{t_m} + \frac{s_e}{(\alpha+\beta)t_m} tanh(\lambda_3 x_r / 2) \tag{24}$$

The addends on the right-hand side of the previous equation are both positive and the stationarity point of Eq. (24) is:

$$x_r^m = \frac{2}{\lambda_3} arcosh\sqrt{\frac{s_e \lambda_3}{2(\alpha+\beta)\tau_r}} \tag{25}$$

The maximum obtainable mortar stress is therefore $\sigma_{m0}^m = \sigma_{m0}(x_r = x_r^m)$. It is also possible that the derivative of σ_{m0} is always negative, for instance, when τ_r is relatively large and/or s_e is relatively small.

If the interface enters the inelastic stage with a $\sigma_{m0}^m < f_{tm}$, mortar can no longer crack and the coupon behaves beyond the elastic limit as described in Case 2.

- Calculation procedure

1) Instant iA

Let us consider that at the Instant (i-1) the interface is fully elastic. At the Instant iA, when at the loaded edge the slip $s_{L_i} > s_e$ and in the centroid $\sigma_{m0}^m \ge f_{tm}$, Case 3 occurs. The transition point x_r at Instant iA (denoted with x_r^{iA}), as shown in Fig. 11-b, can be determined by imposing $\sigma_{m0} = f_{tm}$, and finding with a standard non-linear equations solver the intersection abscissa of the following two curves:

$$\begin{cases} y_1 = f_{tm} - \dfrac{\tau_r(L_i - x_r)}{t_m} \\ y_2 = \dfrac{s_e}{(\alpha+\beta)t_m} tanh(\lambda_3 x_r / 2) \end{cases} \tag{26}$$

The same result can be also conveniently achieved via a spreadsheet varying x_r from L_i to 0, to find the first point that satisfies the condition $\sigma_{m0} \ge f_{tm}$, whose abscissa corresponds to x_r^{iA}. If there are no points satisfying such a condition, mortar can no longer crack. The correctness of Eq. (26) has been verified by the authors in this manner as well. Once that x_r^{iA} is known, the solutions of the elastic and inelastic parts can be determined as described in Case 2.

2) Instant iB

Mortar is cracked at $x' = 0$, see Fig. 11-b; an inelastic phase is active at the interface from x_r^{iA} to L_i . However, what is unknown is the interface status from 0 to x_r^{iA} . Due to the presence of a crack at $x' = 0$, a new plastic zones might appear from 0 to x_r^{iB} . To determine x_r^{iB} , the boundary conditions to impose in the elastic range ($x_{rB}^i \le x \le x_{rA}^i$) for the ODE system are the following:

$$\begin{cases} u_f|_{x=x_r^{iB}} = \dfrac{x_r^{iB}}{E_f}\left(\sigma_f|_{x=x_r^{iB}} - \dfrac{\tau_r x_r^{iB}}{2t_m}\right) \\ (u_f - u_m)|_{x=x_r^{iB}} = -s_e \\ \sigma_m|_{x=x_r^{iB}} = \dfrac{\tau_r x_r^{iB}}{t_m} \\ \sigma_m|_{x=x_r^{iA}} = \dfrac{\tau_r(L_i - x_r^{iA})}{t_m} \end{cases} \tag{27}$$

In which the first condition comes from equilibrium considerations in the part from 0 to x_{rB}^i (similar to the derivation in Eq. (18).), knowing that at $x = 0$, $u_f = 0$. The condition $(u_f - u_m)|_{x=x_r^{iA}} = s_e$ cannot be used since the slip value at x_r^i after the formation of the crack is not necessarily equal to s_e . In fact, the plastic range starts from x_r^{iA} only because the part beyond it has already entered the plastic range in Instant A. Gradually increasing the value of x_r^{iB} from 0 to $L_i/2$, we look for the value that satisfies the condition that the fiber displacement at L_i is equal

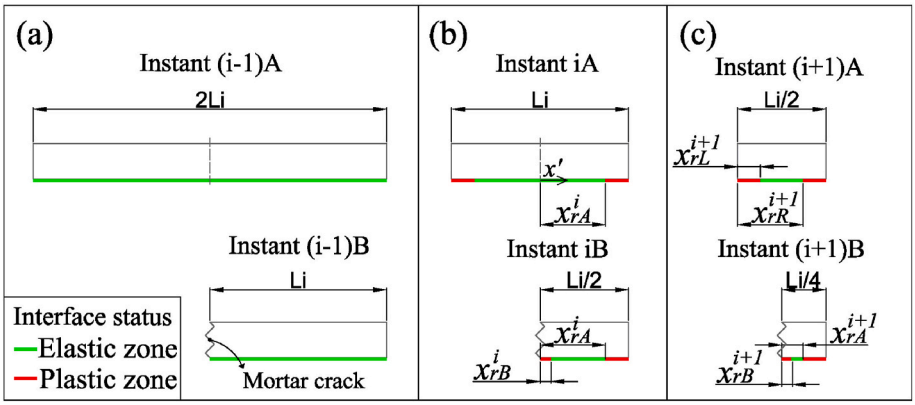

Fig. 11. Schematic calculation procedure of the interface plastic zone in Case 3 at Instant (i-1) (a), instant i (b) and Instant (i+1) (c).

to that of Instant iA (remembering that there is no change in the fiber displacement at the loaded edge passing from Instant A to Instant B), thus obtaining the solution on the whole mortar layer; the solution for the part corresponding to the crack formed in Instant iA can also be easily obtained using symmetry considerations.

3) Instant (i+1)A

If the current length of the uncracked specimen still allows the formation of cracks inside the mortar ($\sigma_{m0}^{m} \geq f_{tm}$), and the tensile ultimate strength of the fiber has not been reached ($\sigma_{fLi} < f_{tf}$), the calculation for Case 3 needs to be repeated. Passing from Instant iB to (i+1)A, the method to determine the inelastic range is different, considering that the interface is already partially plastic. The new elastic range is shown in Fig. 11-c and spans from x_{rL}^{i+1} to x_{rR}^{i+1} .

First, similar to the approach of searching x_r^{iB} in Instant iB, without expanding the plastic range on the right ($x_{rR}^{i+1} = x_r^{iA}$), the value of x_{rL}^{i+1} is gradually increased. The boundary conditions to use in the elastic part include Eq. (28). It is then evaluated that value of x_{rL}^{i+1} between x_r^{iB} and $L_i/2$ that satisfies the condition that the maximum tensile stress of the mortar layer is equal to the mortar tensile strength:

$$\begin{cases} u_f\big|_{x=x_{rL}^{i+1}} = \dfrac{x_{rL}^{i+1}}{E_f}\left(\sigma_f\big|_{x=x_{rL}^{i+1}} - \dfrac{\tau_r x_{rL}^{i+1}}{2t_m}\right) \\ \left(u_f - u_m\right)\big|_{x=x_{rL}^{i+1}} = -s_e \\ \sigma_m\big|_{x=x_{rL}^{i+1}} = \dfrac{\tau_r x_{rL}^{i+1}}{t_m} \\ \sigma_m\big|_{x=x_{rR}^{i+1}} = \dfrac{\tau_r\left(L_i - x_{rR}^{i+1}\right)}{t_m} \end{cases} \tag{28}$$

Another possible situation is that, it may happen that for any value of x_{rL}^{i+1} , the tensile strength is not attained, which means that the plastic range of the interface expands. For a given value of x_{rR}^{i+1} (decreasing from x_r^{iA}), it is then found the value of x_{rL}^{i+1} that satisfies the continuity condition of the mortar stress, as well as the condition that the slip at the interface reaches the elastic limit at both ends of the central elastic zone. Obviously, if the plastic zone is symmetric around the centroid, the boundary conditions to impose are also symmetric and the solution can be obtained; in this case, the maximum mortar stress appears in correspondence with the center of symmetry. In the authors' experience when training with such a cumbersome procedure, the plastic zone appears symmetrically; and even if the interface enters the inelastic phase, the development of the plastic zone is generally small. The above calculations have been carried out in Matlab (but a common spreadsheet can be used as well) with a search length for the parameters involved equal to 0.01 mm, which appears sufficiently accurate for the problems of technical relevance discussed in the paper. Finally, the calculations for Instants (i+1)B can be performed as discussed for the previous Instant iB.

The algorithm is iterated until the rupture of the fiber, which occurs in the model always at the loaded edges. The failure point for the specimen can be determined similarly to what was done in Instants iA, only replacing the boundary condition written for the maximum mortar stress with a new one on the value of the fiber stress. The calculation procedure followed is reported in the synoptic flow chart of Fig. 12.

5.2. Examples and discussions

Three sets of interface parameters (reported in Table 4) are considered to have an insight into the sensitivity of the results obtainable with the model proposed.

Fig. 13 shows the three sets of interface parameters considered, location, and the number of cracks observed in the model with a mortar tensile strength equal to 3.65 MPa. Blue circles refer to Set 2, black

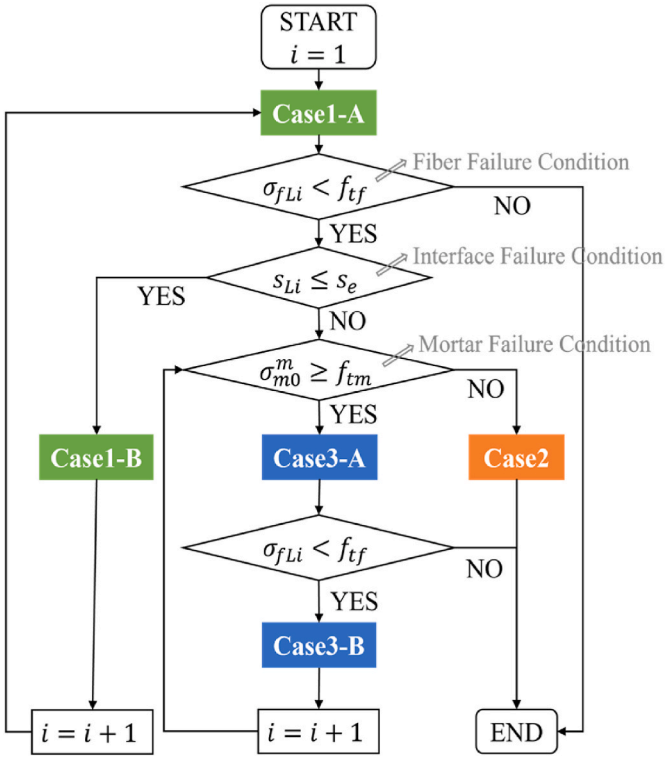

Fig. 12. Flowchart to calculate FRCM coupon behavior under tension considering various failure mechanisms.

Table 4
Interface parameters adopted for Case 3.

Sets	shear strength τ_m [MPa]	stiffness K_i [N/mm^3]	elastic slip limit s_e [mm]	residual strength τ_r [MPa]
Set 1	2.5	166.67	0.015	0.25
Set 2	2.5	166.67	0.015	0.5
Set 3	3.5	233.33	0.015	0.5

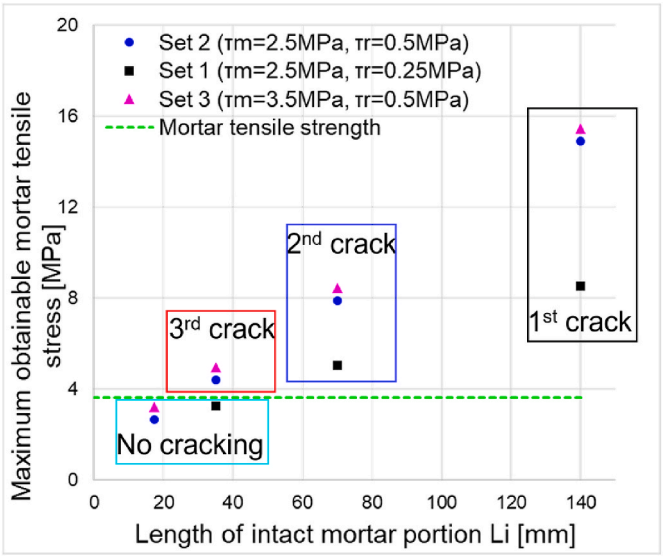

Fig. 13. Comparisons of maximum obtainable mortar stress σ_{m0}^{m} and mortar tensile strength under different L_i.

squares to Set 1, and magenta triangles to Set 3. The judgments of mortar cracking are made based on the comparison between σ_{m0}^{m} and f_{tm} under different L_i, as presented in the previous section. In particular, as visible also in Fig. 14, three cracks can be identified for Set 2 and Set 3, in which larger values of τ_r are adopted, compared to Set 1 (only two cracks can be formed). Fig. 14 shows the global stress-slip curves obtained with the different sets of parameters, superimposed with experimental data. Zoomed details at the initial stage of the loading process (stages 1 and 2 of the trilinear idealized curve) are also reported for the sake of clearness.

In Fig. 15, the distributions of the internal variables -e.g. mortar stress, interface slip, and shear stress-along the coupon length (one-half of the specimen is represented and Set 2 results are considered) at different instants are reported. The symmetric behavior is pretty evident, as well as the location of cracks in the mortar layer and the extension of the plastic zone inside the interface. Considering the global behavior (Fig. 14) and the local one (Fig. 15), it can be deduced that although the number and location of the cracks are different, the stress-strain curves obtained for the coupon are pretty similar. In particular, the elastic phases (stage 1) exhibit the same stiffness; as expected, with a larger τ_m, the elastic phase is longer; in the second stage, the fiber stress before and after the appearance of the cracks inside the mortar is not much different, as well as the extension of the phase; the third stage is, as expected, characterized by a stiffness close to that of the dry fiber textile.

In order to provide additional validation of the effectiveness of the model proposed, some comparisons with results obtained experimentally in Ref. [3] for the other two groups of coupons (made with Glass G-FRCM and Carbon C-FRCM) are also reported. The mechanical properties adopted in the simulations are summarized in Table 5. Similar to the previous determination of interface parameters for the PBO group, the interface peak tangential stress τ_m is kept equal to 75% of the mortar tensile strength, the elastic limit s_e is set equal to 0.015 mm, and a residual strength equal to 20% of τ_m is assumed. Fig. 16 presents the results obtained using the model named Case 3; experimental tests refer to Glass and Carbon groups. It can be seen that there is a good agreement between numerical predictions and experimental evidence for all groups (including the PBO group, reported in Fig. 14): the main features of the trilinear constitutive relationships are well reproduced, the numerical strain and stress values in the second stage are close to the

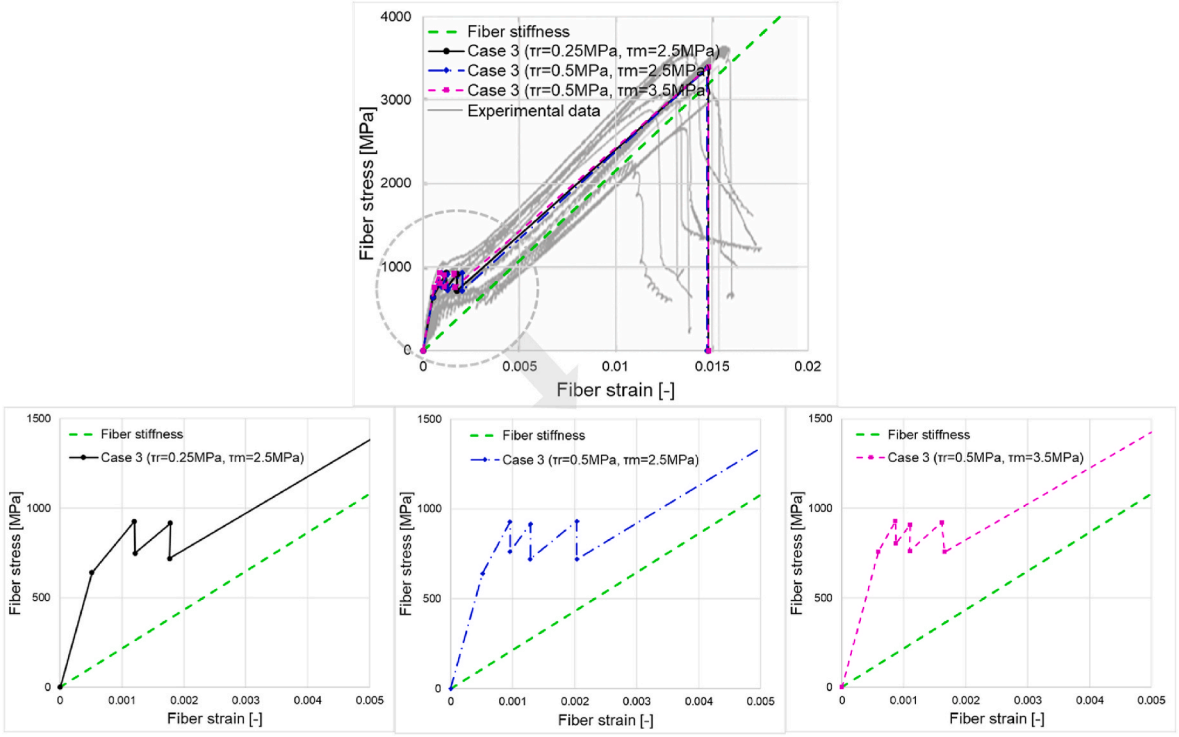

Fig. 14. Global stress-strain curves obtained for Case 3 assuming different residual strengths at the interface, and comparisons with experimental data.

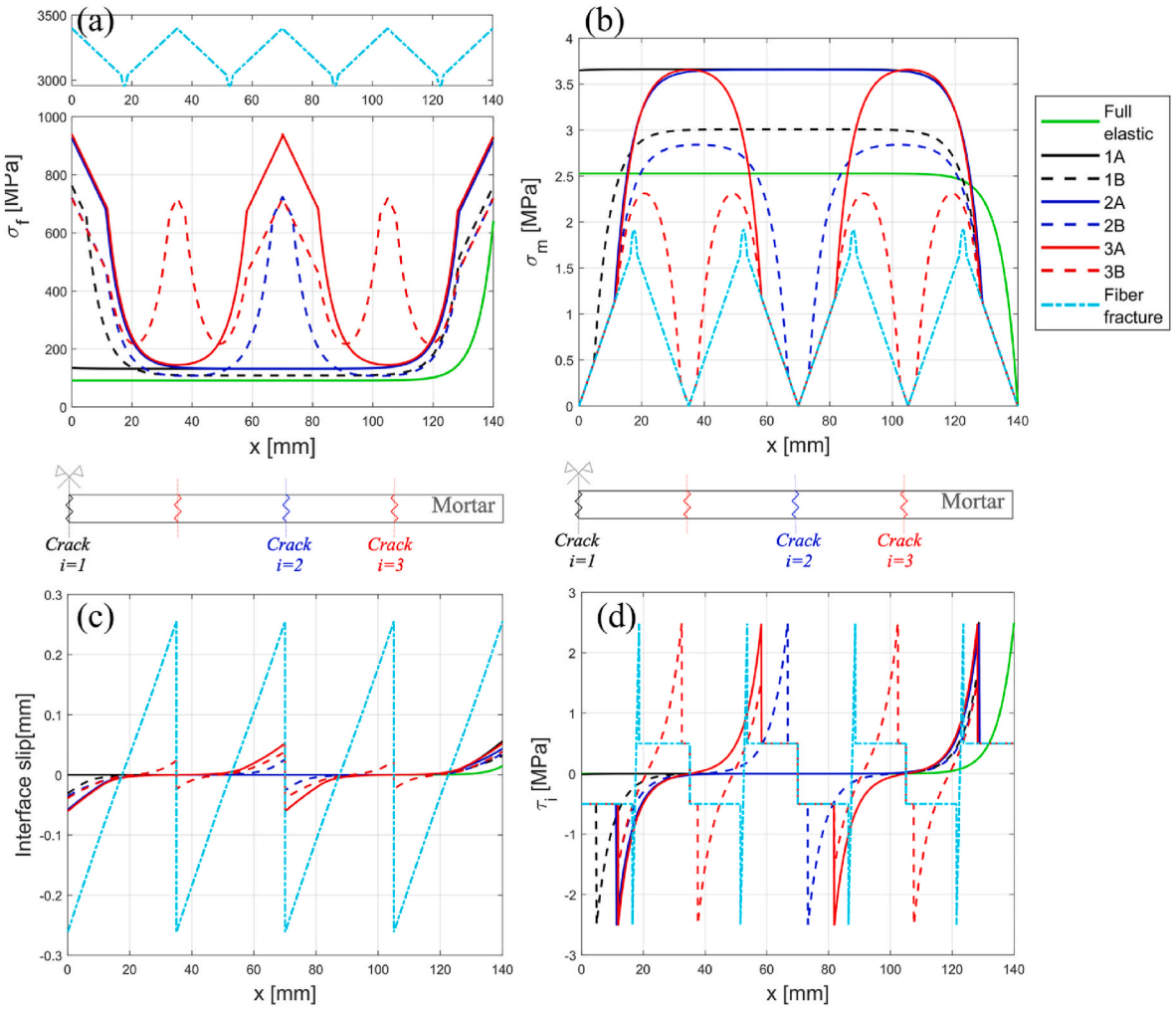

Fig. 15. Case 3 (Set 2): Distribution of (a) fiber tensile stress, (b) mortar tensile stress, (c) interface slip and (d) shear stress until fiber rupture.

Table 5
Parameters adopted for G-FRCM and C-FRCM groups.

Component	Parameter	Symbol and unit	Value	
			Glass-FRCM	Carbon-FRCM
Mortar	Young's modulus	E_m [MPa]	8000	7000
	thickness (one layer)	t_m [mm]	5	5
	tensile strength	f_{tm} [MPa]	2.07	2.02
Fiber textile	Young's modulus	E_f [MPa]	55600	203000
	equivalent thickness	t_f [mm]	0.045	0.042
	length	L [mm]	280	280
	width	B [mm]	40	40
	tensile strength	f_{tf} [MPa]	1121	1913
Interface	shear strength	τ_m [MPa]	1.5	1.5
	stiffness	K_i [N/mm^3]	100	100
	elastic slip limit	s_e [mm]	0.015	0.015
	residual strength	τ_r [MPa]	0.3	0.3

experimental one, and the stiffness in the third stage provided by the analytical model is very near to that of the dry textile tested, as expected (see Fig. 16).

Considering all the models proposed in the paper (Case 1, Case 2, and Case 3), it can be stated that all of them allow reproducing the global stress-strain curves in a quite satisfactory manner when compared with the experimental data, despite the simplifications introduced to handle the analytical solutions. Comparatively speaking:

- Cases 1 and 3 consider mortar damage, hence they allow also a quite precise characterization of the typical phenomena of stiffness degradation occurring in stage 2 in the trilinear curve, and the oscillatory behavior observed experimentally. The differences between the results obtained when the matrix layer is assumed elastic-brittle while the interface is elastic (Case 1) and when both the interface and mortar are assumed inelastic (Case 3) are not detectable from the global stress-strain curves, since in both cases several oscillations of the stress are visible in the second stage. In fact, the exact sequence of the cracks' appearance inside the mortar and the inelasticity triggering at the interface turn out to be strongly dependent on the mechanical properties adopted in the model for the matrix and interface.
- Case 2 ignores the occurrence of cracks in the mortar layer, a hypothesis that does not allow clearly identifying the occurrence of the second stage; in agreement with intuition, an underestimation of the specimen ductility when the value of the interface residual strength is high can be observed.
- All Cases in the third stage exhibit stiffness close to that of the dry fiber textile, but differently from what was observed experimentally, in Case 1 cracks continue to open also in this stage because no interface damage is possible.

It should be also noted that the prediction of the crack locations

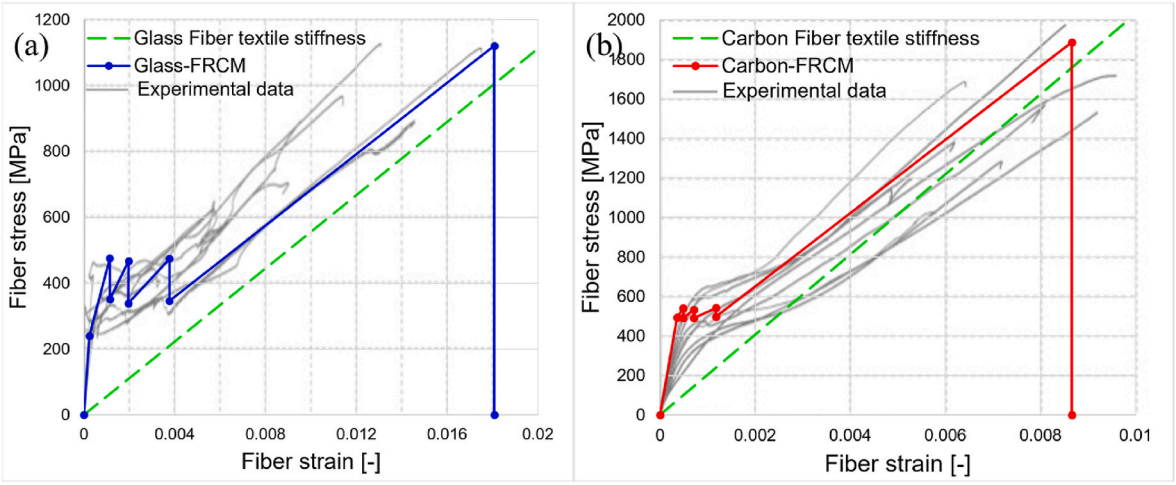

Fig. 16. Global stress-strain relationships of Case 3 for (a) Glass-FRCM group and (b) Carbon-FRCM group, and comparisons with experimental data.

provided by this model is purely conventional and cannot be considered predictive of the actual experimental results, which are unavoidably influenced by many uncertainties. In agreement with such practical consideration, more complex numerical models where different material properties at different locations are assigned (according to a stochastic approach) may be required, similar to what is already presented in some specialized literature [30,31].

- Saturation crack spacing

For Case 3, where more complex failure mechanisms are involved, it is also interesting to discuss the occurrence and location of mortar cracks by means of a comparison between the so-called saturation crack spacing (L^s) and the length provided by the model (L_i). It is interesting to observe that Eq. (25). provides values of x_r^m independent from L_i. The minimum length L^s that allows the formation of a concentrated crack inside mortar can be gained via Eq. (24). assuming $\sigma_{m0}^m = f_{tm}$:

$$L^s = \frac{f_{tm}t_m}{\tau_r} - \frac{s_e}{(\alpha+\beta)\tau_r} tanh\left(\frac{\lambda_3 x_r^m}{2}\right) + x_r^m \tag{29}$$

For the mechanical and geometric properties used in the present simulations, L^s is equal to 42.4 mm, 27.4 mm, and 21.8 mm for Sets 1 to 3 separately, values fully consistent with those predicted by Case 3.

- Inelastic zone propagation inside the interface

The role played by the inelastic region in Case 3 is to gradually expand in order to achieve mortar cracking. However, as shown in Fig. 15, the plastic zone hardly develops with the increase of cracks. If we consider the plastic zone to develop symmetrically, Eq. (24) can as well be utilized to determine gradually the plastic zone extension when mortar cracks; indeed, it is possible to write the following relation:

$$f_{tm} = \frac{\tau_r(L_i - x_r)}{t_m} + \frac{s_e}{(\alpha+\beta)t_m} tanh(\lambda_3 x_r / 2) \tag{30}$$

By observing the second term, it is possible to deduce that, when $(\lambda_3 x_r / 2)$ is large enough, the value of $tanh(\lambda_3 x_r / 2)$ tends to one, so the length of the plastic zone $(L_i - x_r)$ is almost constant and equal to the following expression:

$$L_i - x_r \cong \frac{f_{tm}t_m}{\tau_r} - \frac{\tau_r s_e}{(\alpha+\beta)} \tag{31}$$

It is useful to remember that x_r denotes the local coordinate in Instants i of the transition point on the right between elastic and inelastic behavior of the interface, the value of which is normally large at the early stages of cracking. Moreover, when the external load applied increases, x_r becomes shorter, and mortar can no longer crack, because the length where the interface is able to transfer stresses from the fiber to the mortar layer is not sufficiently long. With the data used in the present simulations and considering $\tau_r = 0.2\tau_m$, if $x_r \cong 20$ mm, the term $tanh(\lambda_3 x_r / 2)$ is about 0.96, while the saturation crack spacing L^s is 27.4 mm (to compare with $L_i = L_3 = 35\ mm$). The above considerations are graphically represented in Fig. 17, where curves y_1 and y_2 of Eq. (26) are depicted; we should also mention that the same results of x_r have been obtained by the authors with a Matlab implementation.

- Occurrence of different cases

In the model, only the extension of the plastic zone and displacements are related to the previous step; when the plastic zone extension is known, stresses and interfacial slip distributions are only dependent on the properties of the components and the length of the analyzed portion. Moreover, the conditions for determining whether the interface (inequality of Eq. (20)) and mortar fail are also related to the component properties and the length of the analyzed sub-coupon. Keeping the properties of mortar and fibers as in Table 1, as well as the interface elastic stiffness constant, for different values of s_e and τ_r, Cases 1, 2 and 3

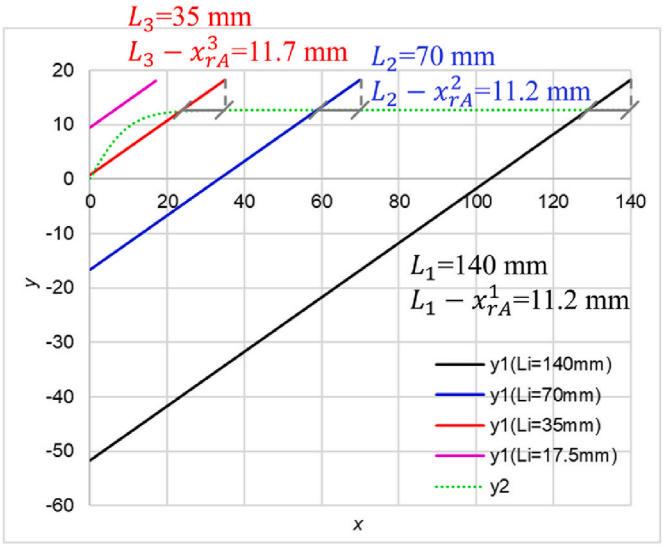

Fig. 17. Prediction of the extension of the inelastic zone in Case 3 for Set 2 data.

occur at different values of L/L_i ratio, as depicted in Fig. 18. In the horizontal axis the ratio L/L_i is represented, the vertical axis is s_e and the subplots refer to different values of τ_r. In addition, an increase of the horizontal coordinate indicates a decreasing length of the analyzed sub-coupon (and indirectly the position of a mortar crack).

It can be seen that the threshold where an interface inelastic behavior is observed is higher when s_e is larger, and Case 1 occurs more often. Case 2 appears later when τ_r gets larger, which means that the number of mortar cracks appearing during the whole loading process increases (and the saturation crack length is shorter) when the interface residual strength is sufficiently high.

6. Conclusions

An analytical model to describe the mechanical behavior of FRCM coupons in tension has been presented. Interfacial damage, mortar cracking, and the simultaneous occurrence of both mortar cracking and mortar/fiber interface inelastic behavior have been extensively discussed. The present model has been focused on the condition where mortar first cracks appear early near the edges of the clamping grip devices. The simple mathematical formulation proposed has been based on considering a mortar layer and a fiber textile (assumed always elastic until rupture) subjected to tension and exchanging at the interface tangential stresses. The setup of an experimental clevis grip test has not been investigated in detail (it will be discussed in future dedicated research) because it plays a meaningful role only at the first stages of the deformation process. Indeed, if the assumption that the initial cracks will appear near the grips is made, the afterward analyses are similar for both the clamping and clevis gripping systems. A major difference is that, for the clevis gripping system, additional assumptions about the shear stress distribution between the steel plate and the mortar (for example, as assumed in the literature [25]), and a quite complex calculation of the internal actions transferred by the steel plate to the fiber textile are required to deduce the global stress-strain curve. Such considerations go beyond the possibilities of the present approach, which is mono-dimensional and on purpose disregards the local multi-dimensional state of stresses with the aim of deriving analytical formulas.

Three cases have been discussed in detail: in Case 1, an elastic brittle behavior for mortar has been assumed to maintain the interface elastic, in Case 2 the interface has been considered non-linear (elastic-perfectly brittle with residual strength) and mortar elastic, whereas in Case 3 both mortar and interface have been assumed non-linear. In Case 1, two sub-models have been extensively discussed (called respectively Case 1-a and Case 1-b); in Case 1-a mortar has been assumed elastic-perfectly brittle, whereas in Case 1-b an exponential softening model has been considered to describe the crack opening. In Case 2, the interface has been assumed to behave in an elastic-perfectly brittle manner with residual tangential strength. The role played by such residual resistance has been extensively discussed in the numerical examples analyzed to validate the analytical model proposed.

Under the aforementioned assumptions, it has been possible -by writing the equilibrium equations for mortar and fiber layers-to deduce an ODE system admitting closed-form solution. Different cases -such as crack formation inside mortar and evolution of slippage at the interface fiber/mortar-has required to impose different boundary conditions and to analyze different portions of the coupon (e.g. between two contiguous cracks), depending on the cases, which has allowed an analytical determination of stresses and displacements during the entire deformation process.

It has been shown that the model can satisfactorily reproduce the trilinear constitutive law assumed in the engineering practice for the speedy characterization of the behavior of coupons subjected to tensile tests. As far as the global behavior (in terms of applied load and measured deformation) is concerned, all models have proved a very satisfactory agreement with experimental evidence. Locally (i.e. to predict the formation of cracks and slippage along the coupon length), the results obtained have also shown that it is necessary to consider the

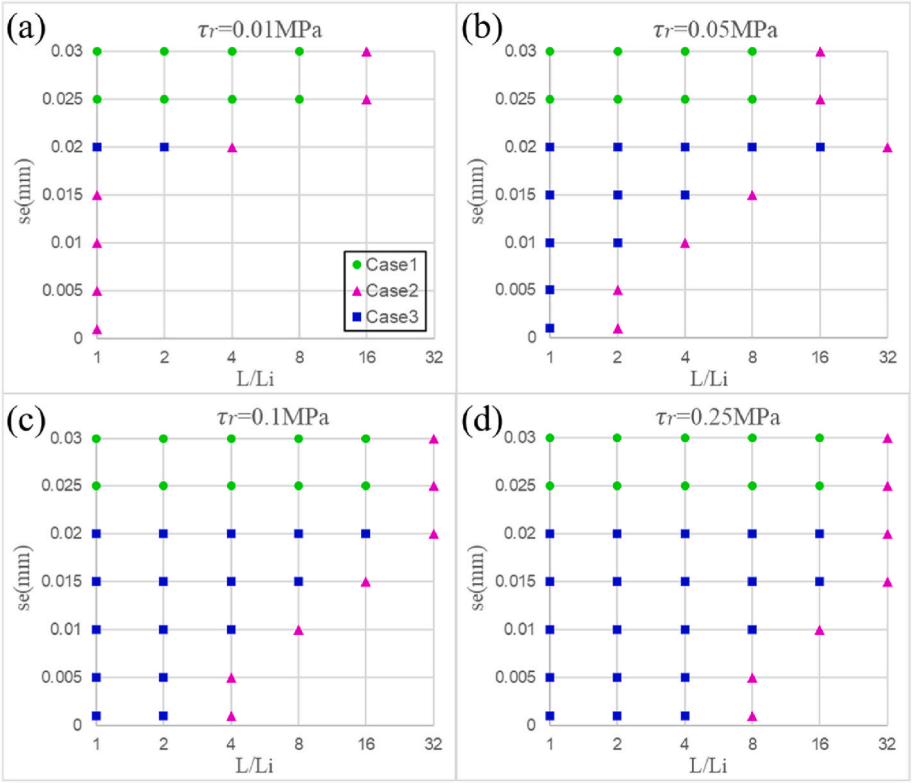

Fig. 18. Occurrence of different cases while changing interface parameters (s_e and τ_r) under different analysis lengths L_i.

simultaneous failure of mortar and interface to avoid the formation of unrealistic cracks inside mortar at short coupon lengths. A sensitivity analysis carried out changing the interface elastic limit and the residual strength has put in evidence that there is a certain influence on the failure mechanisms triggered, although the global stress-strain response found has been pretty similar in all the cases investigated.

The simplicity of the approach, its reliability and the very limited computational burden required (almost all the analyses carried out are based on a closed-form formulation) make the model particularly attractive to explain in an easy way some typical phenomena occurring in FRCM tensile tests, the most important being for sure the contemporary damage of mortar and interface. Further developments of the proposed model include its application to the study of (i) single lap shear tests, (ii) entire reinforced structural elements in- and out-of-plane loaded, and (iii) reinforced curved masonry pillars, the latter being a topic particularly important for the strengthening of arches and vaults.

CRediT authorship contribution statement

Yu Yuan: Conceptualization, Methodology, Investigation, Validation, Data curation, Writing – original draft. **Gabriele Milani:** Conceptualization, Methodology, Investigation, Validation, Data curation, Writing – original draft, Supervision.

Declaration of competing interest

The authors declare that they have no known competing financial interests or personal relationships that could have appeared to influence the work reported in this paper.

Data availability

Data will be made available on request.

References

[1] Donnini J, de Caso y Basalo F, Corinaldesi V, Lancioni G, Nanni A. Fabric-reinforced cementitious matrix behavior at high-temperature: experimental and numerical results. Compos B Eng 2017;108:108–21. https://doi.org/10.1016/j.compositesb.2016.10.004.

[2] Calabrese AS, D'Antino T, Colombi P. Experimental and analytical investigation of PBO FRCM-concrete bond behavior using direct and indirect shear test set-ups. Compos Struct 2021;267:113672. https://doi.org/10.1016/j.compstruct.2021.113672.

[3] Carozzi FG, Poggi C. Mechanical properties and debonding strength of Fabric Reinforced Cementitious Matrix (FRCM) systems for masonry strengthening. Compos B Eng 2015;70:215–30. https://doi.org/10.1016/j.compositesb.2014.10.056.

[4] CNR - Advisory Committee on Technical Recommendations for Construction. CNR-DT 215/2018, guide for the design and construction of externally bonded fibre reinforced inorganic matrix systems for strengthening existing structures. 2020.

[5] ACI Committee. ACI 549.4 R-20, guide to design and construction of externally bonded fabric-reinforced cementitious matrix and steel-reinforced grout systems for repair and strengthening of concrete structures. 2020.

[6] D'Anna J, Amato G, Chen JF, Minafò G, la Mendola L. Experimental application of digital image correlation for the tensile characterization of basalt FRCM composites. Construct Build Mater 2021;271:121770. https://doi.org/10.1016/j.conbuildmat.2020.121770.

[7] Bellini A, Bovo M, Mazzotti C. Experimental and numerical evaluation of fiber-matrix interface behaviour of different FRCM systems. Compos B Eng 2019;161:411–26. https://doi.org/10.1016/j.compositesb.2018.12.115.

[8] Larrinaga P, Chastre C, Biscaia HC, San-José JT. Experimental and numerical modeling of basalt textile reinforced mortar behavior under uniaxial tensile stress. Mater Des 2014;55:66–74. https://doi.org/10.1016/j.matdes.2013.09.050.

[9] Bertolesi E, Fagone M, Rotunno T, Grande E, Milani G. Experimental characterization of the textile-to-mortar bond through distributed optical sensors. Construct Build Mater 2022;326:126640. https://doi.org/10.1016/j.conbuildmat.2022.126640.

[10] D'Antino T, Papanicolaou C. Comparison between different tensile test set-ups for the mechanical characterization of inorganic-matrix composites. Construct Build Mater 2018;171:140–51. https://doi.org/10.1016/j.conbuildmat.2018.03.041.

[11] D'Antino T, Papanicolaou C. Mechanical characterization of textile reinforced inorganic-matrix composites. Compos B Eng 2017;127:78–91. https://doi.org/10.1016/j.compositesb.2017.02.034.

[12] de Santis S, Hadad HA, de Caso y Basalo F, de Felice G, Nanni A. Acceptance criteria for tensile characterization of fabric-reinforced cementitious matrix systems for concrete and masonry repair. J Compos Construct 2018;22. https://doi.org/10.1061/(ASCE)CC.1943-5614.0000886.

[13] Donnini J, Corinaldesi V. Mechanical characterization of different FRCM systems for structural reinforcement. Construct Build Mater 2017;145:565–75. https://doi.org/10.1016/j.conbuildmat.2017.04.051.

[14] de Domenico D, Maugeri N, Longo P, Ricciardi G, Gullì G, Calabrese L. Clevis-grip tensile tests on basalt, carbon and steel FRCM systems realized with customized cement-based matrices. Journal of Composites Science 2022;6:275. https://doi.org/10.3390/jcs6090275.

[15] Donnini J, Corinaldesi V, Nanni A. Mechanical properties of FRCM using carbon fabrics with different coating treatments. Compos B Eng 2016;88:220–8. https://doi.org/10.1016/j.compositesb.2015.11.012.

[16] Leone M, Aiello MA, Balsamo A, Carozzi FG, Ceroni F, Corradi M, et al. Glass fabric reinforced cementitious matrix: tensile properties and bond performance on masonry substrate. Compos B Eng 2017;127:196–214. https://doi.org/10.1016/j.compositesb.2017.06.028.

[17] Carozzi FG, Bellini A, D'Antino T, de Felice G, Focacci F, Hojdys Ł, et al. Experimental investigation of tensile and bond properties of Carbon-FRCM composites for strengthening masonry elements. Compos B Eng 2017;128:100–19. https://doi.org/10.1016/j.compositesb.2017.06.018.

[18] Lignola GP, Caggegi C, Ceroni F, de Santis S, Krajewski P, Lourenço PB, et al. Performance assessment of basalt FRCM for retrofit applications on masonry. Compos B Eng 2017;128:1–18. https://doi.org/10.1016/j.compositesb.2017.05.003.

[19] de Santis S, Ceroni F, de Felice G, Fagone M, Ghiassi B, Kwiecień A, et al. Round Robin test on tensile and bond behaviour of steel reinforced grout systems. Compos B Eng 2017;127:100–20. https://doi.org/10.1016/j.compositesb.2017.03.052.

[20] Caggegi C, Carozzi FG, De Santis S, Fabbrocino F, Focacci F, Hojdys Ł, et al. Experimental analysis on tensile and bond properties of PBO and aramid fabric reinforced cementitious matrix for strengthening masonry structures. Compos B Eng 2017;127:175–95. https://doi.org/10.1016/j.compositesb.2017.05.048.

[21] Caggegi C, Lanoye E, Djama K, Bassil A, Gabor A. Tensile behaviour of a basalt TRM strengthening system: influence of mortar and reinforcing textile ratios. Compos B Eng 2017;130:90–102. https://doi.org/10.1016/j.compositesb.2017.07.027.

[22] Tekieli M, de Santis S, de Felice G, Kwiecień A, Roscini F. Application of digital image correlation to composite reinforcements testing. Compos Struct 2017;160:670–88. https://doi.org/10.1016/j.compstruct.2016.10.096.

[23] Arboleda D, Carozzi FG, Nanni A, Poggi C. Testing procedures for the uniaxial tensile characterization of fabric-reinforced cementitious matrix composites. J Compos Construct 2016;20. https://doi.org/10.1061/(ASCE)CC.1943-5614.0000626.

[24] Focacci F, D'Antino T, Carloni C. Tensile testing of FRCM coupons for material characterization: discussion of critical aspects. J Compos Construct 2022;26. https://doi.org/10.1061/(ASCE)CC.1943-5614.0001223.

[25] Focacci F, D'Antino T, Carloni C. The role of the fiber–matrix interfacial properties on the tensile behavior of FRCM coupons. Construct Build Mater 2020;265:120263. https://doi.org/10.1016/j.conbuildmat.2020.120263.

[26] Grande E, Milani G, Imbimbo M. Theoretical model for the study of the tensile behavior of FRCM reinforcements. Construct Build Mater 2020;236:117617. https://doi.org/10.1016/j.conbuildmat.2019.117617.

[27] Minafò G, Oddo MC, la Mendola L. Formulation of a truss element for modelling the tensile response of FRCM strips. Construct Build Mater 2022;315:125576. https://doi.org/10.1016/j.conbuildmat.2021.125576.

[28] Monaco A, Minafò G, D'Anna J, Oddo MC, la Mendola L. Constitutive numerical model of FRCM strips under traction. Front Built Environ 2020;6. https://doi.org/10.3389/fbuil.2020.00060.

[29] Grande E, Milani G. Procedure for the numerical characterization of the local bond behavior of FRCM. Compos Struct 2021;258:113404. https://doi.org/10.1016/j.compstruct.2020.113404.

[30] Grande E, Milani G. Numerical simulation of the tensile behavior of FRCM strengthening systems. Compos B Eng 2020;189:107886. https://doi.org/10.1016/j.compositesb.2020.107886.

[31] Bertolesi E, Carozzi FG, Milani G, Poggi C. Numerical modeling of fabric reinforce cementitious matrix composites (FRCM) in tension. Construct Build Mater 2014;70:531–48. https://doi.org/10.1016/j.conbuildmat.2014.08.006.

[32] Aveston J, Kelly A. Theory of multiple fracture of fibrous composites. J Mater Sci 1973;8:352–62. https://doi.org/10.1007/BF00550155.

[33] Oddo MC, Minafo G, La Mendola L. Constitutive models for the tensile behaviour of TRM materials: literature review and experimental verification. Materials 2021;14:17. https://doi.org/10.3390/ma14030700.

[34] Mobasher B, Pahilajani J, Peled A. Analytical simulation of tensile response of fabric reinforced cement based composites. Cem Concr Compos 2006;28:77–89. https://doi.org/10.1016/j.cemconcomp.2005.06.007.

[35] Nerilli F, Ferracuti B. A tension stiffening model for FRCM reinforcements calibrated by means of an extended database. Compos Struct 2022;284:115100. https://doi.org/10.1016/j.compstruct.2021.115100.

[36] Donnini J, Lancioni G, Corinaldesi V. Failure modes in FRCM systems with dry and pre-impregnated carbon yarns: experiments and modeling. Compos B Eng 2018;140:57–67. https://doi.org/10.1016/j.compositesb.2017.12.024.

[37] Zhu M, Zhu J-H, Ueda T, Matsumoto K, Su M. Bond behavior of carbon fabric reinforced cementitious matrix (FRCM) composites considering matrix impregnation. Compos Struct 2021;262:113350. https://doi.org/10.1016/j.compstruct.2020.113350.

[38] Carozzi FG, Milani G, Poggi C. Mechanical properties and numerical modeling of Fabric Reinforced Cementitious Matrix (FRCM) systems for strengthening of masonry structures. Compos Struct 2014;107:711–25. https://doi.org/10.1016/j.compstruct.2013.08.026.
[39] Mobasher B, Peled A, Pahilajani J. Distributed cracking and stiffness degradation in fabric-cement composites. Mater Struct 2007;39:317–31. https://doi.org/10.1007/s11527-005-9005-8.
[40] Wang J, Jivkov AP, Li QM, Engelberg DL. Experimental and numerical investigation of mortar and ITZ parameters in meso-scale models of concrete. Theor Appl Fract Mech 2020;109:102722. https://doi.org/10.1016/j.tafmec.2020.102722.
[41] Lourenço PB, Rots JG. Multisurface interface model for analysis of masonry structures. J Eng Mech 1997;123:660–8. https://doi.org/10.1061/(ASCE)0733-9399(1997)123:7(660).
[42] Van der Pluijm R. Material properties and its components under tension and shear. In: Proc., 6th can. Masonry symp.; 1992. Saskatoon, Canada.